Non-Hermitian chiral phononics through optomechanically-induced squeezing

Javier del Pino[1,2,*] Jesse J. Slim[1,*] Ewold Verhagen[1]

[1]Center for Nanophotonics, AMOLF, Science Park 104, 1098 XG Amsterdam, The Netherlands
[2]Institute for Theoretical Physics, ETH Zürich, 8093 Zürich, Switzerland
[*] J. d. P. and J. J. S. contributed equally to this work.

Imposing chirality on a physical system engenders unconventional energy flow and responses, such as the Aharonov-Bohm effect [1] and the topological quantum Hall phase for electrons in a symmetry-breaking magnetic field. Recently, great interest has arisen in combining that principle with broken Hermiticity to explore novel topological phases and applications. [2–16] Here, we report unique phononic states formed when combining the controlled breaking of time-reversal symmetry with non-Hermitian dynamics, both induced through time-modulated radiation pressure forces in small nano-optomechanical networks. We observe chiral energy flow among mechanical resonators in a synthetic dimension and Aharonov-Bohm tuning of their eigenmodes. Introducing particle-non-conserving squeezing interactions, we discover a non-Hermitian Aharonov-Bohm effect in ring-shaped networks in which mechanical quasiparticles experience parametric gain. The resulting complex mode spectra indicate flux-tuning of squeezing, exceptional points, instabilities and unidirectional phononic amplification. This rich phenomenology points the way to exploring new non-Hermitian topological bosonic phases and applications in sensing and transport that exploit spatiotemporal symmetry breaking.

From the Zeeman to the quantum Hall effect, magnetic fields biasing electronic systems alter their spectrum and imprint chirality on their eigenstates. Nonreciprocal interference underlies these phenomena, as electrons travelling along a closed path gain a phase proportional to the enclosed magnetic flux that depends on direction — evidencing broken time-reversal ($\mathcal{T}$) symmetry. Such geometrical phases [1] and the resulting synthetic magnetism were recently brought to bosonic systems in photonics, acoustics, and cold atoms to explore nonreciprocal functionality [17–20] and various topological insulators. [21,22]

In a parallel, largely unconnected development, researchers turned to non-Hermitian systems such as parity-time- ($\mathcal{PT}$-)symmetric systems, featuring dynamical phase transitions linked to spectral singularities such as exceptional points (EPs). [23,24] Here, controlled gain and loss lead to unique eigenmode symmetries and tuning of *complex* eigenfrequencies ϵ. Bosonic systems form the natural realm for these phenomena, with lasing and self-oscillation ubiquitous in photonics and mechanics. In particular, bosonic *squeezing* is described by Hamiltonians that do not conserve excitation number, and engender distinct phases showing stable or unboundedly growing dynamics. [25,26]

Very recently, the combination of topology and non-Hermiticity attracted strong interest. [2,3] Tailoring gain and loss in topological insulators showed lasing into protected states [6,7,12] and topological phase transitions. [8] In principle, states with symmetries, dynamics, and spectra that are altogether different from Hermitian chiral systems are expected. [4,5] Indeed, various non-Hermitian topological phases were predicted, with associated chirally-amplified and unstable edge modes, [9–11] quadrature-dependent chiral transport [27,28] and anomalous bulk-boundary correspondence with extreme sensitivity to boundary conditions. [2,13–16] However, the rich combination of squeezing interactions and geometrical phases remained experimentally unexplored so far.

Here we demonstrate Aharonov-Bohm (AB) interference and chirality of nanomechanical states in multi-resonator networks where both $\mathcal{T}$-symmetry-breaking geometrical phases and non-Hermiticity are induced through radiation pressure. Since suitable laser drives stimulate frequency-converting transitions, optomechanical control [29] allows parametric amplification and synthetic magnetism for photons [18,19] and phonons. [30,31] We combine both here, using squeezing interactions in addition to particle-conserving interactions to create non-Hermitian dynamics without dissipation [25,32] and uncover new geometrical phases. Using light to sensitively actuate and detect nanomechanical motion, we reveal the unique effects of this merger on chiral transport, dynamical phases, and squeezing — and actively control them in space and time.

Phononic circulation

We first induce phononic chirality by breaking $\mathcal{T}$ symmetry in a network with Hermitian closed-system dynamics, henceforth simply called *Hermitian*. We disregard the small intrinsic mechanical dissipation in the systems' most basic description, while including it in all relevant calculations (Methods). A sliced photonic crystal

nanobeam[31] supports multiple non-degenerate MHz-frequency flexural mechanical modes coupled to the optical field of a nanocavity. Each mode ('resonator') i changes the cavity frequency by $g_0^{(i)}x_i$ through displacement x_i (normalised to the zero-point amplitude) and experiences a force $\propto g_0^{(i)}n_c$, with $g_0^{(i)}$ the vacuum optomechanical coupling rate and n_c the intracavity photon number. Figure 1a shows distinct mechanical resonances in the thermomechanical noise spectrum, read out as modulations of a detuned probe laser reflected from the cavity (Methods).

While the (uncoupled) mechanical resonators have well-separated eigenfrequencies ω_i, interactions are established by temporal modulation of the intensity of a control laser detuned from cavity resonance. For optimal laser detuning $\Delta = -\kappa/(2\sqrt{3})$, with cavity decay rate κ, mechanical displacement modulates the intracavity intensity instantaneously at phononic timescales ($\kappa \gg \omega_i$). Mixing of a control laser intensity modulation at the difference frequency $\omega_j - \omega_i$ of resonators i and j with the radiation pressure force sideband of resonator i creates a sideband at ω_j. The resulting 'cross-mode optical spring effect'[31] induces particle-conserving beamsplitter coupling between the resonators at rate $J_{ij} = c_{\mathrm{m}} g_i g_j \Delta/(\Delta^2 + \kappa^2/4)$, with $g_i = g_0^{(i)}\sqrt{\bar{n}_c}$ scaling with average cavity population $\bar{n}_c$ and modulation depth c_{m} (Methods).

Three resonators are coupled in a ring network by simultaneously applying three modulation tones (Fig. 1b). Describing the resonators in frames rotating at ω_i, the phonon-number-preserving Hamiltonian for this 'beamsplitter trimer' (BST) reads

$$H_{\mathrm{BST}} = \sum_{i=1,j\neq i}^{3} J_{ij} e^{-i\varphi_{ij}} a_i^\dagger a_j, \qquad \varphi_{ji} = -\varphi_{ij}, \qquad (1)$$

without intrinsic dissipation. This Hamiltonian importantly imprints the modulation phase φ_{ij} in a non-reciprocal fashion on phonons transferred along the loop – precisely like the Peierls phase imprinted by a magnetic vector potential.[31] The gauge-invariant geometrical phase $\Phi = \varphi_{12} + \varphi_{23} + \varphi_{31}$ around the loop then represents a synthetic flux threading the resonator plaquette.

Setting equal $J_{ij} = J$, Hamiltonian (Eq. (1)) is translationally invariant in a gauge with equal Peierls phases, and therefore diagonal in the discrete momentum basis $\tilde{a}_k = \sum_{j=1}^{3} e^{-i2\pi kj/3} a_j/\sqrt{3}$ for $k = \{-1, 0, 1\}$. Through AB interference along the loop, the enclosed flux shifts the eigenfrequencies $\epsilon_k = 2J\cos((2\pi k + \Phi)/3)$. Figure 1c reveals these states in the thermomechanical spectrum, for each resonance splits into a (Floquet) triplet due to strong coupling $J > \gamma_i$, with mechanical damping rates γ_i. This demonstration of nanomechanical flux-tuning is paralleled in spectra of quantum rings under magnetic fields.[33] Note that with homogeneous dissipation ($\gamma_i = \gamma$) closed-system behaviour is recovered for transformed modes $a_i' = a_i e^{\gamma t/2}$.[24]

The flux-tuning manifests AB interference over a given rotation – the mechanism ultimately responsible for chirality of quantum Hall edge states[22] and non-reciprocal dynamics.[33] Figures 1d,e show evolution of a mechanical excitation with chirality controlled by the flux. For $\Phi \in \{0, \pi\}$, the BST is time-reversal symmetric (Methods) and energy simultaneously hops to both other resonators. Any other flux breaks $\mathcal{T}$ symmetry, lifting the degeneracy of opposite momentum eigenstates and enabling chiral energy transport, manifested for $\Phi = \pi/2$ ($\Phi = -\pi/2$) as a clockwise (counterclockwise) circulation.

Non-Hermitian Aharonov-Bohm effect

We thus demonstrated a chiral phononic circulator[34] using light-induced nanomechanical beamsplitter interactions, with scaling potential to topological lattices.[31] Still, vastly richer phenomenology is uncovered by introducing squeezing interactions in the nodes and links of the network, which were not considered in earlier work. We implement single-mode ($i = j$) or two-mode ($i \neq j$) mechanical squeezing by optical modulation at sum-frequency $\omega_i + \omega_j$. The Hamiltonian reads (Methods)

$$H^{\mathrm{sq}} = \sum_{i,j} \frac{\eta_{ij}}{2} (e^{i\theta_{ij}} a_i a_j + e^{-i\theta_{ij}} a_i^\dagger a_j^\dagger), \qquad (2)$$

with interaction strength $\eta_{ij} = c_{\mathrm{m}} g_i g_j \Delta/(\Delta^2 + \kappa^2/4)$ and modulation phase θ_{ij} now imprinted on the creation or annihilation of phonon pairs. Squeezing angles θ_{ij} form a powerful control resource, as the Peierls phases φ_{ij} before. Indeed, spatially patterned squeezing yields anomalous pairing terms, enabling topological bosonic states unparalleled by their fermionic (e.g. topological superconductor) counterparts and is essential for proposed topological amplifiers.[11]

We first consider a 'squeezing dimer' (SD, Fig. 2a) consisting of two resonators, each single-mode squeezed through $2\omega_i$ modulation, and coupled through driving at $\omega_2 - \omega_1$ (Hamiltonian $H_{\mathrm{SD}} = \eta_1 e^{i\theta_1} a_1^2/2 + \eta_2 e^{i\theta_2} a_2^2/2 + J e^{i\varphi_{12}} a_2^\dagger a_1 + \mathrm{H.c.}$). Remarkably, we find that the *level* of squeezing of thermal fluctuations is not only determined by the interactions' magnitude η_i, J, but also by their phases θ_i, φ_{12}. Figure 2b shows single-mode squeezing is maximal when $\varphi_{12} = \pi/2$ and disappears when $\varphi_{12} \in \{0, \pi\}$ if $\theta_1 = \theta_2 = \pi/2$ and $\eta_1 = \eta_2 = \eta$.

We now show that this observation is associated with a *non-Hermitian* version of AB interference. Even though the coupled-mode picture Fig. 2a shows no plaquette, we can recognise a loop along which excitations experience a geometric phase when combining graph representation with Bogoliubov-de Gennes (BdG) formalism.[26] Treating a_i and $a_i^\dagger$ as separate degrees of freedom – 'particles' and 'holes' – and squeezing (Eq. (2)) as particle-hole conversion, this representation (Fig. 2c) reveals for SD a conjugate pair of superimposed loops in particle-hole space, threaded by gauge-invariant fluxes

$\Phi = 2\varphi_{12} - \theta_1 + \theta_2$ and $-\Phi$. As these fluxes govern interference in the loop, they control the connection between the resonators' quadratures (defined such that $X_i = (a_i + a_i^\dagger)/\sqrt{2}$ ($Y_i = i(a_i^\dagger - a_i)/\sqrt{2}$) are squeezed (anti-squeezed) for $J = 0$): While $\Phi = \pi$ connects the squeezed quadratures, maximizing squeezing, $\Phi = 0$ connects squeezed quadrature X_1 to anti-squeezed quadrature Y_2 and vice versa, cancelling the overall squeezing (Fig. 2d, Methods).

Flux-controlled $\mathcal{PT}$ symmetry

This geometric phase again impacts normal mode frequencies. These are now generally complex – given by the eigenvalues of the BdG dynamical matrix $\mathcal{H}_{\rm SD}$ defining the closed-system equations of motion $i\dot{\vec{\alpha}} = \mathcal{H}_{\rm SD}\vec{\alpha}$, where $\vec{\alpha} = (a_1, a_2, a_1^\dagger, a_2^\dagger)$ (Methods). Even without dissipation ($\gamma_i = 0$), squeezing makes $\mathcal{H}_{\rm SD}$ necessarily non-Hermitian, preserving only Σ_z-pseudo-Hermiticity ($\Sigma_z = {\rm diag}(\mathbb{1}, -\mathbb{1})$, $\mathcal{H}_{\rm SD}^\dagger = \Sigma_z\mathcal{H}_{\rm SD}\Sigma_z$) to satisfy bosonic commutation relations.[26] AB-like interference in the BdG loop thus acquires a non-Hermitian character, where now frequency *and* linewidth evolve with flux. In the strongly coupled, dynamically stable regime ($J > \eta$, $2\eta < \gamma_i$, Fig. 2e,f), Φ strongly tunes linewidth and thermal amplitude of the hybridised eigenmodes, in unison with squeezing. The squeezed and antisqueezed partners recognised for $\Phi = \pi$ in Fig. 2d correspond to broad and narrow resonances, respectively,[35] with the latter dominating the spectrum (Methods).

The complex eigenvalues define surfaces in $J/\eta - \Phi$ space (Fig. 3a), with varying degeneracy, indicating distinct dynamical phases. Their physical properties are appreciated by studying the dynamical matrix in the quadrature basis $\mathcal{H}_{\rm SD}^{XY}$. For $\Phi = 0$, $\mathcal{H}_{\rm SD}^{XY}$ respects $\mathcal{P}_{X_iY_j}\mathcal{T}$-symmetry for the two degenerate "quadrature dimers" $X_iY_{j\neq i}$ (Fig. 2d), where $\mathcal{P}_{X_iY_j}$ exchanges $X_i \leftrightarrow Y_j$. We thus demonstrate $\mathcal{PT}$-symmetric physics by means of squeezing dynamics, instead of coupling to dissipative baths.[25,32] The SD features a pair of complex eigensurfaces, two-fold degenerate in real and imaginary parts. The only effect of non-zero but equal dissipation is a uniform displacement of the dynamical matrix $\mathcal{H}_{\rm SD}^{XY} \to \mathcal{H}_{\rm SD}^{XY} - i\gamma\mathbb{1}/2$ (Methods), manifesting $\mathcal{PT}$ symmetry in the basis $a_i' = a_i e^{\gamma t/2}$, i.e. 'passive' $\mathcal{PT}$ symmetry in the corresponding open system.[24]

The thermomechanical spectra in Fig. 3b evidence the distinct dynamic phases. Along $\Phi = 0$, we recognise behaviour of the conventional $\mathcal{PT}$-symmetric dimer:[24] Eigenmodes (hosted by quadrature dimers) respect $\mathcal{PT}$ symmetry for $J > \eta$, with equal linewidths and splitting increasing with J. For $J < \eta$, $\mathcal{PT}$ symmetry is spontaneously broken, with degenerate frequencies independent of J, while linewidths split (Extended Data Fig. 2). $\mathcal{H}_{\rm SD}$ becomes defective at a degenerate pair of second-order EPs (one per quadrature dimer), when $J = \eta$. Finite fluxes break the $\mathcal{P}_{X_iY_j}\mathcal{T}$ symmetry of $\mathcal{H}_{\rm SD}^{XY}$ explicitly, eliminating EPs for any J or η (Fig. 3b, bottom). The effect of flux is striking for $J \approx \eta$ (Fig. 3c), where we find strong tuning of both frequency and linewidth, with eigenmodes coalescing at the degenerate EPs $\Phi \in \{0, 2\pi\}$.

Higher-order EPs and chiral amplification

The SD behaviour is intrinsically quadrature-dependent, as the paths in quasiparticle space link conjugated elements a_i and $a_i^\dagger$ directly or indirectly. The response to any real excitation (a superposition of a_i's and $a_i^\dagger$'s) then depends on the particle-hole phase difference, i.e. the excited quadrature. Another example is phase-dependent amplification in the bosonic Kitaev chain (without synthetic flux).[26,27] One can, however, conceive loops without such links, expecting quadrature-independent nonreciprocity and chirality (Methods). The Hermitian BST represents a trivial example, comprising two *disjoint* loops connecting all particles and holes, respectively (Fig. 4a).

We find a non-Hermitian system encompassing disjoint loops by 'conjugating' one resonator in the BST, i.e. swapping $a_3 \leftrightarrow a_3^\dagger$. We implement this 'singly conjugated trimer' (SCT) by modulating at $\omega_2 - \omega_1, \omega_1 + \omega_3$ and $\omega_2 + \omega_3$. The latter induce two-mode squeezing, specifically $H_{\rm SCT} = Je^{i\varphi_{12}}a_2^\dagger a_1 + \eta_{23}e^{i\theta_{23}}a_3 a_2 + \eta_{13}e^{-i\theta_{13}}a_1^\dagger a_3^\dagger$ + H.c., and loops threaded by fluxes $\Phi = \varphi_{12} + \theta_{23} - \theta_{13}$ and $-\Phi$ (Fig. 4a).

The disjoint loop topology of the quasiparticle network implies *block-diagonality* of the BdG dynamical matrix $\mathcal{H}_{\rm SCT}$, with non-Hermitian blocks governing each loop's dynamics. The interplay of AB interference and non-Hermiticity in SCT induces dynamical stability transitions, unmatched by BST. Figure 4b shows these as surfaces in $J/\eta - \Phi$ space for $\eta_{13} = \eta_{32} = \eta$ and equal dissipation $\gamma_i = 0$. We identify a stable phase with real eigenfrequencies and an unstable phase with three distinct imaginary parts.

Interestingly, for $J = 2\sqrt{2}\eta$ the (real) eigenvalues of a single loop of $\mathcal{H}_{\rm SCT}$ coincide with those of a homogeneous BST ($J_{ij} = J$) for all Φ. The thermal spectra in Fig. 4c show, however, that the response around ω_3 associated with the 'conjugated' resonator (3) appears frequency-reflected, since particles (holes) evolve with positive (negative) frequencies in the non-rotating frame. Moreover, we observe asymmetries between resonators 1 and 2 in the middle band's thermal amplitude at $\Phi \in \{\pi/2, 3\pi/2\}$. These asymmetric, flux-controlled localisation of fluctuations — unattainable in the BST if $J_{31} = J_{23}$ — arise from the combination of chirality and squeezing and persist even for vacuum fluctuations (Supplementary Information sec. IIF). These asymmetries, akin to chiral, incoherently pumped dynamics in $\mathcal{PT}$-symmetric trimers,[36] suggest the SCT functions like a phononic nonreciprocal amplifier.[11,17,18,20]

We see the SCT features an exceptional *contour* in the $J/\eta - \Phi$ parameter space (Fig. 4b), linked to the spontaneous breaking of parity-time ($\mathcal{P}_{gl}\mathcal{T}$) sym-

metry. Here, the effective mirror symmetry, $\mathcal{P}_{gl}$, exchanges 'gainy' and 'lossy' eigenmodes $a_{g,l}$ for $J = 0$, namely $a_{g,l} = (a_+ \mp i a_3^\dagger)/\sqrt{2}$ with $\epsilon_{g,l} = \pm\sqrt{2}i\eta$ where $a_+ = (a_1 + a_2)/\sqrt{2}$ (gauge $\theta_{ij} = 0$). When $\Phi \in \{0, \pi\}$, a beam-splitter interaction $J > 0$ couples $a_g \leftrightarrow a_l$, constructing a $\mathcal{P}_{gl}\mathcal{T}$-symmetric dimer with a second order EP at $J = 2\sqrt{2}\eta$ (Fig. 4d, top). However, for $\Phi \in \{\pi/2, 3\pi/2\}$, a third, neutral mode $a_- = (a_1 - a_2)/\sqrt{2}$ — uncoupled when $\Phi \in \{0, \pi\}$ — couples to $a_{l,g}$ in a loss-neutral-gain chain configuration. Interestingly, this trimer features spontaneous $\mathcal{P}_{gl}\mathcal{T}$ symmetry breaking at a *third-order* EP at $J = \sqrt{2}\eta$ (Fig. 4d bottom). Indeed, the presence of a higher-order EP sitting at the nexus of two second-order exceptional contours[37] is mandated by eigensurface topology (Fig. 4b).

The flux-induced breaking of $\mathcal{P}_{12}$ (mirror) symmetry impacts specifically the $\mathcal{P}_{gl}\mathcal{T}$-symmetry-broken phase. In a three-site, gainy-neutral-lossy chain, $\mathcal{PT}$-symmetry-broken states delocalise non-uniformly over central and boundary sites (here the pairs $a_g - a_-$ and $a_- - a_l$).[38] Crossing the third-order EP at $\Phi = \pm\pi/2$ thus biases gain towards the bare oscillator a_1 ($\Phi = \pi/2$) or a_2 ($\Phi = -\pi/2$). This flux-tunable chiral gain becomes striking in the transient, unstable dynamics of the SCT, as shown in Fig. 4e for gain exceeding dissipation. There, an initial excitation in resonator 1 (2) is amplified coherently – above initial amplitudes – towards 2 (1) for flux $\Phi = \pi/2$ ($\Phi = -\pi/2$), and attenuated quickly in the opposite direction. Conversely, for $\Phi = 0$, gain distributes evenly over resonators 1 and 2 showing reciprocal dynamics. Linear analysis breaks down as the system crosses the instability threshold ($\mathrm{Im}(\epsilon) = 0$), where we see optomechanically-induced Duffing nonlinearities cause amplitude saturation and self-oscillations, even at only a few times the thermal amplitude. Indeed, this points the way to investigating strongly nonlinear systems with broken Hermiticity and time-reversal symmetry.

In conclusion, we observed chiral, non-Hermitian phonon dynamics in nano-optomechanical networks with fully-controlled beamsplitter and squeezing interactions. New geometrical phases act on excitations in particle-hole space that control $\mathcal{PT}$ symmetry through a non-Hermitian Aharonov-Bohm effect. The resulting phenomena of tunable squeezing, (higher-order) EPs and nonreciprocal amplification point to applications in nanomechanical sensing,[39], signal processing,[11], and Ising machines.[40] These mechanisms will be equally powerful in other bosonic domains, from photonics to cold atoms. While the effects were probed with thermal and coherent excitations, they persist down to the quantum domain, forming essential ingredients to explore new linear and nonlinear non-Hermitian topological phases.

[1] Cohen, E. *et al.* Geometric phase from Aharonov-Bohm to Pancharatnam-Berry and beyond. *Nat. Rev. Phys.* **1**, 437–449 (2019).

[2] Bergholtz, E. J., Budich, J. C. & Kunst, F. K. Exceptional topology of non-Hermitian systems. *Rev. Mod. Phys.* **93**, 015005 (2021).

[3] Coulais, C., Fleury, R. & van Wezel, J. Topology and broken Hermiticity. *Nat. Phys.* **17**, 9–13 (2021).

[4] Lieu, S. Topological symmetry classes for non-Hermitian models and connections to the bosonic Bogoliubov-de Gennes equation. *Phys. Rev. B* **98**, 115135 (2018).

[5] Gong, Z. *et al.* Topological phases of non-Hermitian systems. *Phys. Rev. X* **8**, 031079 (2018).

[6] St-Jean, P. *et al.* Lasing in topological edge states of a one-dimensional lattice. *Nat. Photonics* **11**, 651–656 (2017).

[7] Hu, B. *et al.* Non-Hermitian topological whispering gallery. *Nature* **597**, 655–659 (2021).

[8] Zeuner, J. M. *et al.* Observation of a topological transition in the bulk of a non-Hermitian system. *Phys. Rev. Lett.* **115**, 040402 (2015).

[9] Barnett, R. Edge-state instabilities of bosons in a topological band. *Phys. Rev. A* **88**, 063631 (2013).

[10] Peano, V., Houde, M., Brendel, C., Marquardt, F. & Clerk, A. A. Topological phase transitions and chiral inelastic transport induced by the squeezing of light. *Nat. Commun.* **7**, 10779 (2016).

[11] Peano, V., Houde, M., Marquardt, F. & Clerk, A. A. Topological quantum fluctuations and traveling wave amplifiers. *Phys. Rev. X* **6**, 1–17 (2016).

[12] Bandres, M. A. *et al.* Topological insulator laser: Experiments. *Science* **359**, eaar4005 (2018).

[13] Ghatak, A., Brandenbourger, M., van Wezel, J. & Coulais, C. Observation of non-hermitian topology and its bulk–edge correspondence in an active mechanical metamaterial. *Proc. Natl Acad. Sci. USA* **117**, 29561–29568 (2020).

[14] Helbig, T. *et al.* Generalized bulk,Äìboundary correspondence in non-Hermitian topolectrical circuits. *Nat. Phys.* **16**, 747–750 (2020).

[15] Weidemann, S. *et al.* Topological funneling of light. *Science* **368**, 311–314 (2020).

[16] Wang, K. *et al.* Generating arbitrary topological windings of a non-Hermitian band. *Science* **371**, 1240–1245 (2021).

[17] Sliwa, K. M. *et al.* Reconfigurable Josephson circulator/directional amplifier. *Phys. Rev. X* **5**, 041020 (2015).

[18] Ruesink, F., Miri, M.-A., Alù, A. & Verhagen, E. Nonreciprocity and magnetic-free isolation based on optomechanical interactions. *Nat. Commun.* **7**, 13662 (2016).

[19] Fang, K. *et al.* Generalized non-reciprocity in an optomechanical circuit via synthetic magnetism and reservoir engineering. *Nat. Phys.* **13**, 465–471 (2017).

[20] Mercier de Lépinay, L., Ockeloen-Korppi, C. F., Malz, D. & Sillanpää, M. A. Nonreciprocal transport based on cavity Floquet modes in optomechanics. *Phys. Rev. Lett.* **125**, 023603 (2020).

[21] Huber, S. D. Topological mechanics. *Nat. Phys.* **12**, 621–623 (2016).

[22] Ozawa, T. *et al.* Topological photonics. *Rev. Mod. Phys.* **91**, 015006 (2019).

[23] Miri, M.-A. & Alù, A. Exceptional points in optics and photonics. *Science* **363** (2019).

[24] Özdemir, Ş. K., Rotter, S., Nori, F. & Yang, L. Parity-time symmetry and exceptional points in photonics. *Nat. Mater.* **18**, 783–798 (2019).

[25] Wang, Y. X. & Clerk, A. A. Non-Hermitian dynamics without dissipation in quantum systems. *Phys. Rev. A* **99**, 063834 (2019).

[26] Flynn, V. P., Cobanera, E. & Viola, L. Deconstructing effective non-Hermitian dynamics in quadratic bosonic Hamiltonians. *New J. Phys.* **22**, 083004 (2020).

[27] McDonald, A., Pereg-Barnea, T. & Clerk, A. A. Phase-dependent chiral transport and effective non-Hermitian dynamics in a bosonic Kitaev-Majorana chain. *Phys. Rev. X* **8**, 041031 (2018).

[28] Wanjura, C. C., Brunelli, M. & Nunnenkamp, A. Topological framework for directional amplification in driven-dissipative cavity arrays. *Nat. Commun.* **11**, 3149 (2020).

[29] Aspelmeyer, M., Kippenberg, T. J. & Marquardt, F. Cavity optomechanics. *Rev. Mod. Phys.* **86**, 1391–1452 (2014).

[30] Xu, H., Jiang, L., Clerk, A. A. & Harris, J. G. E. Nonreciprocal control and cooling of phonon modes in an optomechanical system. *Nature* **568**, 65–69 (2019).

[31] Mathew, J. P., del Pino, J. & Verhagen, E. Synthetic gauge fields for phonon transport in a nano-optomechanical system. *Nat. Nanotechnol.* **15**, 198–202 (2020).

[32] Koutserimpas, T. T. & Fleury, R. Non-reciprocal gain in non-Hermitian time-Floquet systems. *Phys. Rev. Lett.* **120**, 087401 (2017).

[33] Roushan, P. *et al.* Chiral ground-state currents of interacting photons in a synthetic magnetic field. *Nat. Phys.* **13**, 146–151 (2017).

[34] Habraken, S. J., Stannigel, K., Lukin, M. D., Zoller, P. & Rabl, P. Continuous mode cooling and phonon routers for phononic quantum networks. *New J. Phys.* **14**, 115004 (2012).

[35] Huber, J. S. *et al.* Spectral evidence of squeezing of a weakly damped driven nanomechanical mode. *Phys. Rev. X* **10**, 021066 (2020).

[36] Downing, C. A., Zueco, D. & Martín-Moreno, L. Chiral current circulation and PT symmetry in a trimer of oscillators. *ACS Photonics* **7**, 3401–3414 (2020).

[37] Tang, W. *et al.* Exceptional nexus with a hybrid topological invariant. *Science* **370**, 1077–1080 (2020).

[38] Hodaei, H. *et al.* Enhanced sensitivity at higher-order exceptional points. *Nature* **548**, 187–191 (2017).

[39] Lau, H.-K. & Clerk, A. A. Fundamental limits and non-reciprocal approaches in non-Hermitian quantum sensing. *Nat. Commun.* **9**, 4320 (2018).

[40] Mahboob, I., Okamoto, H. & Yamaguchi, H. An electromechanical Ising Hamiltonian. *Sci. Adv.* **2**, e1600236 (2016).

Figure 1: Aharonov-Bohm interference in a Hermitian nano-optomechanical network. a Thermomechanical fluctuation spectrum of the sliced photonic crystal nanobeam, imprinted on a laser reflected from a nanocavity with linewidth $\kappa/(2\pi) = 320$ GHz. Resonances forming a synthetic dimension correspond to mechanical flexural modes at frequencies $\omega_i/(2\pi) = \{3.7, 5.3, 12.8, 17.6\}$ MHz with loss rates $\gamma_i/(2\pi) \approx 1-4$ kHz and estimated vacuum optomechanical coupling rates $g_0^{(i)}/(2\pi) = \{5.3, 5.9, 3.3, 3.1\}$ MHz. **b** The modulated cavity field c couples the three lowest-frequency resonators in a loop with rates $J_{ij}/(2\pi) = 8$ kHz and Peierls phases φ_{ij}, adding up to flux Φ. These coupling strengths are achieved with modulation depths c_m between 0.32 and 0.42, at mean photon number $\bar{n}_c \approx 343$. **c** Thermomechanical noise spectra imprinted on the detection laser around each resonator's sideband versus flux. Hybridised Floquet modes tune with synthetic flux. **d** Time evolution of resonator amplitudes $|\langle a_i \rangle| \equiv |a_i|$ for unbroken $\mathcal{T}$ symmetry ($\Phi = 0$) and broken ($\Phi = \pi/2$). Resonator a_1 is coherently driven until $t = 0$ ms through resonantly modulated radiation pressure, when excitation is stopped and modulation tones implementing the couplings are established. **e** Time evolution of resonator amplitudes for varying flux, showing crossover from helical to non-helical transport through an intermediate regime with generally aperiodic dynamics, and reversal of chirality with flux sign ($\Phi \mapsto -\Phi$). ESD, energy spectral density. For reference, the optomechanical coupling routinely reaches experimental cooperativities $C_{ij} = (4J_{ij}^2/(\gamma_i\gamma_j)) > 80$, allowing two-mode transfer efficiencies $\approx 70\%$ (Extended Data Fig. 1).

Figure 2: AB interference along non-Hermitian squeezing loops: **a** The squeezing dimer encompasses two resonators driven at $2\omega_i$ and $\omega_2 - \omega_1$. These introduce single-mode nanomechanical squeezing (blue self-loops) and beam-splitter coupling (red). We employ the modes labeled (3) and (4) in Fig. 1a as resonator 1 and 2, respectively. **b** Histograms of the steady-state phase space distribution of resonator 1 for varying beamsplitter Peierls phase φ_{12}, showing its effect on thermomechanical squeezing. Dashed ellipses depict the standard deviation of the principal components of the quadrature covariance matrix. Here $\theta_1 = \theta_2 = \pi/2$. **c** Graph associated to the Hamiltonian matrix (Methods Eq. 3), unwrapping self-loops in **a** over particles (annihilated by a_i) and holes (annihilated by $a_i^\dagger$). The clockwise loop is threaded by synthetic flux Φ, the counterclockwise by $-\Phi$. **d** Coupling diagram for resonator quadratures, where Φ controls coupling between squeezed (green) and anti-squeezed (orange) quadratures of the two resonators. **e** Thermomechanical spectra for the SD around ω_1. **f** Sweeping flux continuously tunes the fitted apparent resonance linewidths $\gamma_{I,II}$ (blue and red circles), compared to the theoretical loss rate of the lowest-loss eigenfrequency of $\mathcal{H}_{\mathrm{SD}}$ (solid black). **g** Flux-dependent level of squeezing, measured as the ratio of the variances $\Delta R^2_{\mathrm{sq.}}$ and $\Delta R^2_{\mathrm{a.}}$ of the quadratures squeezed and antisqueezed along the principal axes of the covariance matrix, respectively, in experiment (green) and theory (dashed, Supplementary Information sec. II A and sec. II B). Here, $J/(2\pi) = 5.37$ kHz, $\eta_1/(2\pi) = \eta_2/(2\pi) = 1.34$ kHz, and loss rates $\gamma_1/(2\pi) \approx \gamma_2/(2\pi) = 3.7$ kHz. ESD, energy spectral density. Error bars in **f** (**g**) are dominated by fitting (statistical) uncertainties, with a small contribution from control parameter fluctuations (Methods).

Figure 3: Flux-control of non-Hermitian dynamical phases. a Complex eigenfrequency surfaces of the SD in $J - \Phi$ space for $\gamma_i = 0$, tuned by the non-Hermitian AB effect acting on its beamsplitter and squeezing links. For $\Phi \in \{0, 2\pi\}$ and $\eta = J$, $\mathcal{PT}$ symmetry breaks spontaneously and the eigenspectrum coalesces into two second order EPs. **b** Fingerprints of complex degeneracies in the thermomechanical spectra for resonator 1 at $\eta/(2\pi) = 1.34$ kHz and varying J. Nonzero flux breaks $\mathcal{P}_{X_iY_j}\mathcal{T}$ symmetry explicitly, precluding EPs. **c** Flux-tuned spectra for resonator 1 when $J/(2\pi) \approx \eta/(2\pi) = 1.34$ kHz, showing mode coalescence at the EP at $\Phi \in \{0, 2\pi\}$. For **b** and **c**, theory eigenvalues $\mathrm{Re}(\epsilon)$ are shown as dashed lines. In this experiment, resonances 3 and 4 have been used, employing dynamical backaction to equilibrate damping rates to $\gamma_i/(2\pi) = 3.7$ kHz (Methods). Fits of frequencies and linewidths are shown in Extended Data Fig. 2.

Figure 4: Chirality in a non-Hermitian network. a Sketch of the networks in particle-hole space corresponding to the BST (left) and the SCT (right), manifesting their topological resemblance. **b** Complex eigensurfaces for the SCT ($\gamma_i = \gamma$) depicted from $\Phi = 0$ to $\Phi = \pi$ for clarity. Imaginary parts are referenced to γ. A black dotted line highlights an exceptional contour separating stable and unstable dynamical phases. **c** Thermomechanical spectra of the three resonators (label denoted in the plot) for $\eta/(2\pi) = 1$ kHz, $J = 2\sqrt{2}\eta$. Feedback is employed to equalise mechanical loss rates $\gamma_i/(2\pi) = \gamma/(2\pi) = 4$ kHz. The sideband of the 'conjugated' resonator 3 is reflected in frequency compared to the other two. Localisation of eigenstates is observed, including 1-2 asymmetry indicated by arrows. Theoretical eigenfrequencies are shown as dashed lines. **d** Spectra for resonators 1 and 3 for $\eta/(2\pi) = 0.75$ kHz for a trivial flux $\Phi = 0$, and in the maximally chiral case $\Phi = \pi/2$. The flux-dependent coupling topology for resonators 1 and 2 morphs a second order EP into a third order one (see text). Insets show the effective $\mathcal{P}_{gl}\mathcal{T}$ symmetric dimer/trimer structure for both flux values. **e** Ratio between instantaneous and initial coherent amplitudes (normalized to phonon number), in the unstable and nonlinear regime $\eta/(2\pi) = J/(2\pi) = 5$ kHz, without feedback (mechanical loss rates $\gamma_i/(2\pi) = \{2.5, 1.6, 4.1\}$ kHz). Resonator 1 (left) or 2 (right) is driven for $t < 0$, and couplings are established when $t > 0$. This induces chirally amplified transport to the other resonator and self-oscillation bounded by nonlinear dynamics.

Methods

Effective mechanical Hamiltonian

We present a comprehensive theoretical model for the optomechanically-mediated nanomechanical interactions in our platform. A cavity mode with frequency ω_c and photon loss rate κ is coupled to an ensemble of mechanical modes with frequencies ω_i (index $i \in \{1, 2\cdots, N\}$) with vacuum optomechanical coupling rates $g_0^{(i)}$, according to the Hamiltonian

$$\tilde{H}_s = \sum_i \omega_i \tilde{a}_i^\dagger \tilde{a}_i - \Delta c^\dagger c - \sum_i g_0^{(i)} c^\dagger c(\tilde{a}_i + \tilde{a}_i^\dagger). \quad \text{(3a)}$$

Here, mechanical annihilation operators in the lab frame are denoted by $\tilde{a}_i$ and we set $\hbar = 1$. Operators $\tilde{a}_i$ correspond to distinct mechanical eigenmodes ('resonators'), which form a *synthetic dimension* along which we study mode hybridisation and excitation transport.[41,42] The cavity field annihilation operator c is expressed in the rotating frame of a control field at frequency ω_L detuned by $\Delta = \omega_L - \omega_c$ from the cavity resonance. We operate in the regime of large detuning and bandwidth ($\Delta, \kappa \gg \omega_i$). With cavity in-coupling rate $\kappa_{\rm in}$, a control field with slowly-varying amplitude $c_{\rm in}(t)$ addresses the intracavity photon population instantaneously, displacing the cavity mode by a steady-state amplitude approximated by the $g_0^{(i)} = 0$ solution

$$\bar{c}(t) \approx \sqrt{\kappa_{\rm in}}\chi_c c_{\rm in}(t), \quad \text{(3b)}$$

with bare cavity susceptibility $\chi_c = (\frac{\kappa}{2} - i\Delta)^{-1}$. Typical values for $\kappa_{\rm in}$ and average optical power $\langle P\rangle_t = \hbar\omega_L \langle |c_{\rm in}(t)|\rangle_t^2$ lie in the range of $\kappa_{\rm in} \approx 0.03\kappa$ and $\langle P\rangle_t = 1.0$ mW, respectively.

We linearise the radiation-pressure interaction Eq. (3a) by displacing the cavity amplitude around Eq. (3b), i.e. $c(t) \to \bar{c}(t) + \delta c(t)$ and neglecting terms $\mathcal{O}((\delta c)^2)$, assuming small cavity fluctuations $\delta c(t)$. In a subsequent step, we find an effective phononic Hamiltonian by carrying out a second-order perturbation treatment to the linearised interaction, consisting of adiabatic elimination of the fluctuations δc through the approach in [43]. This approximation is valid provided cavity fluctuations reach a steady-state of low amplitude at the fastest timescale of the system, as prescribed by $\kappa, \Delta \gg \omega_i$. The detailed procedure can be found in Supplementary Information Sec. IA. In rotating frames at ω_i, accessed via unitary transformation $U_F = e^{-it\sum_i \omega_i \tilde{a}_i^\dagger \tilde{a}_i}$, mechanical operators read $a_i = U_F \tilde{a}_i U_F^\dagger = e^{i\omega_i t}\tilde{a}_i$. Moreover, the effective phononic Hamiltonian $U_F \tilde{H}_{\rm eff} U_F^\dagger = H_{\rm eff} = H_g + H_{\rm eff}^{\rm int}$, decomposes into a displacement term $H_g = -|\bar{c}(t)|^2(\sum_i g_0^{(i)}(a_i e^{-i\omega_i t} + \text{H.c.}))$ and the interaction Hamiltonian

$$H_{\rm eff}^{\rm int} \approx \Delta\kappa_{\rm in}|\chi_c|^4 |c_{\rm in}(t)|^2 \left[\sum_i g_0^{(i)}(a_i e^{-i\omega_i t} + \text{H.c.})\right]^2. \quad \text{(3c)}$$

We introduce modulation of the control field intensity $|c_{\rm in}(t)|^2$ using multiple harmonic driving tones l with frequencies $\omega_{\rm m}^{(l)}$, modulation depths $c_{\rm m}^{(l)}$ and phases $\phi_{\rm m}^{(l)}$. The homogeneous intracavity intensity responds linearly as (Eq. (3b)) $n_c(t) \approx |\bar{c}(t)|^2 = \bar{n}_c\left[1 + \sum_l c_{\rm m}^{(l)} \cos\left(\omega_{\rm m}^{(l)} t + \phi_{\rm m}^{(l)}\right)\right]$, where $\bar{n}_c = \kappa_{\rm in}|\chi_c|^2|\bar{C}_{\rm in}|^2$ is the average photon number.

In the next step, we apply the Rotating Wave Approximation (RWA), which only retains the *co-rotating* terms with slow evolution in the rotating frame. The RWA assumes moderate couplings compared with natural oscillation frequencies and narrow mechanical linewidth $\gamma_i \ll \omega_i$. Considering dynamical modulations are not resonant with any vibrational mode ($\omega_{\rm m}^{(l)} \neq \omega_i$), the relevant contributions in Eq. (3c) thus read $H_{\rm eff}^{\rm int} \approx \sum_{i,j} H_{\rm eff}^{(i,j)}$ with $i, j \in \{1, 2, \cdots N\}$,

$$H_{\rm eff}^{(i,j)} = g(t)(a_i e^{-i\omega_i t} + \text{H.c.})(a_j e^{-i\omega_j t} + \text{H.c.}), \quad \text{(3d)}$$

and $g(t) = \Delta|\chi_c|^2 g_0^{(i)} g_0^{(j)} n_c(t)$. The static component of $n_c(t)$ is responsible for an optical shift of the mechanical spring constant by $\omega_i \mapsto \omega_i + \delta\omega_i$ that is reabsorbed in the definition of ω_i, where $\delta\omega_i = 2g_i^2\Delta/(\Delta^2 + \kappa^2/4)$ and $g_i = g_0^{(i)}\sqrt{\bar{n}_c}$ denotes the cavity-enhanced optomechanical coupling rate.[29] Crucially, the time-dependent part in Eq. (3d) corresponds to mechanical interactions which can be selected by suitably resonant modulation tones l, while imprinting $\phi_{\rm m}^{(l)}$ as a *Peierls* phase on the interaction.[31,44] Within a subsequent RWA, the remaining interaction terms in Eq. (3d) correspond to the modulation frequencies $\omega_{\rm m}^{(l)}$ either approaching a *i)* frequency sum $\Sigma\omega^{\langle ij\rangle} = \omega_i + \omega_j$ or a *ii)* frequency difference $\Delta\omega^{\langle ij\rangle} = \omega_i - \omega_j$, with $i, j \in \{1, 2\cdots, N\}$. The RWA is valid for moderate effective coupling strengths $J_{ij}, \eta_{ij} \ll \omega_i$, defined below (in the experiment, $J_{ij}/\omega_i, \eta_{ij}/\omega_i \sim 10^{-3} - 10^{-2}$), resolved-mechananical sidebands (in the experiment, $\gamma_i/\omega_i \sim 10^{-3} - 10^{-2}$) and moderate detuning of the control tones, as well as no commensurable frequency scales ($\omega_i \pm \omega_j \neq \omega_k$ for all modes i, j, k). Equation 3a finally approximates to

$$H_{\rm eff} \approx \sum_{\omega_{\rm m}^{(l)} \approx \Delta\omega^{\langle ij\rangle}} J_{ij} a_i^\dagger a_j e^{-i[(\omega_{\rm m}^{(l)} - \Delta\omega^{\langle ij\rangle})t + \varphi_{ij}]} + \text{H.c.} + \sum_{\omega_{\rm m}^{(l)} \approx \Sigma\omega^{\langle ij\rangle}} \eta_{ij} a_i^\dagger a_j^\dagger e^{-i[(\omega_{\rm m}^{(l)} - \Sigma\omega^{\langle ij\rangle})t + \theta_{ij}]}/2 + \text{H.c.}, \quad \text{(4a)}$$

where the sums run over the tones l and indices $\langle i, j\rangle$ that satisfy the specified resonance condition. Note that a single pair of indices $\langle i, j\rangle$ satisfies resonance with a difference frequency $\Delta\omega^{\langle ij\rangle}$, while resonance with a sum frequency $\Sigma\omega^{\langle ij\rangle}$ is satisfied by both $\langle i, j\rangle$ and $\langle j, i\rangle$.

The hopping (squeezing) amplitudes, denoted J_{ij} (η_{ij}), are proportional to the modulation depth $c_{\rm m}^{(l)}$ of the corresponding drive tone l[31,45] and read

$$\{J_{ij}, \eta_{ij}\} = c_{\rm m}^{(l)} \frac{g_i g_j \Delta}{(\Delta^2 + \kappa^2/4)} = c_{\rm m}^{(l)} \frac{\sqrt{\delta\omega_i \delta\omega_j}}{2}. \quad \text{(4b)}$$

In the fast-cavity limit photon losses thus simply renormalise the coupling amplitudes J_{ij}, η_{ij}. Similarly, the hopping (squeezing) phases, denoted φ_{ij} (θ_{ij}), are equal to the corresponding modulation phase $\phi_{\mathrm{m}}^{(l)}$.

Besides moderate effective coupling, the RWA relies on the assumption that the modulated drive is quasi-resonant with each relevant process. In the large detuning and parametric drive limit, significant deviations are expected.[46] Parametric resonators are more naturally treated in this case in terms of the natural amplitudes x[47,48] or employing quadratures in a generalised rotating frame.[49] For modulation frequencies resonant with $\Delta\omega^{\langle ij\rangle}, \Sigma\omega^{\langle ij\rangle}$, Eq. (4a) is exactly time-independent. In this limit, we encode the beam-splitter interactions that conserve the phonon number $n_{\mathrm{ph}} = \sum_{i=1}^{N} a_i^\dagger a_i$ in the elements $\mathcal{A}_{ij} = J_{ij} e^{-i\varphi_{ij}}$, $\mathcal{A}_{ji} = \mathcal{A}_{ij}^*$ of the Hermitian *hopping matrix* $\mathcal{A}$. Subsequently, we define the symmetric *squeezing matrix* $\mathcal{B}$ that encodes the particle-non-conserving squeezing interactions in its elements $\mathcal{B}_{ij} = \eta_{ij} e^{i\theta_{ij}}$, $\mathcal{B}_{ji} = \mathcal{B}_{ij}$. Eq. (4a) then writes succinctly as the general quadratic form

$$H_{\mathrm{eff}} \approx \sum_{i,j} a_i^\dagger \mathcal{A}_{ij} a_j + \frac{1}{2}(a_i^\dagger \mathcal{B}_{ij} a_j^\dagger + a_i \mathcal{B}_{ij}^* a_j). \qquad (4c)$$

The matrices $\mathcal{A}$ and $\mathcal{B}$ are provided for the example systems studied in the main text explicitly in Supplementary Information Sec. IC.

Bogoliubov-de-Gennes framework and symmetries

The effective (time-independent) Hamiltonian in the rotating frame Eq. (4c) allows for a straightforward application of the toolbox of quadratic bosonic Hamiltonians. After defining the Nambu-like vector $\vec{\alpha} = (\vec{a}, \vec{a}^\dagger)^T$, with $\vec{a} = (a_1, \cdots, a_N)$, Eq. (4c) is rewritten as

$$H_{\mathrm{eff}} = \frac{1}{2}\vec{\alpha}^\dagger H \vec{\alpha}, \qquad H = \begin{pmatrix} \mathcal{A} & \mathcal{B} \\ \mathcal{B}^* & \mathcal{A}^* \end{pmatrix}. \qquad (5)$$

To faithfully model the ubiquitous mechanical dissipation and thermal fluctuations in the experiment, we introduce coupling to N independent environmental baths in a Heisenberg-Langevin formalism.[50] The corresponding equation of motion for mechanical modes, namely $\dot{\vec{\alpha}}(t) = -i\mathcal{M}\vec{\alpha}(t) + \vec{\alpha}_{\mathrm{in}}(t)$, depends on the open-system dynamical matrix $\mathcal{M} = \mathcal{H} - i\Gamma/2$, containing the dissipation matrix $\Gamma = \mathrm{diag}(\gamma_1, \cdots, \gamma_N, \gamma_1, \cdots, \gamma_N)$, and the BdG dynamical matrix[51,52]

$$\mathcal{H} = \Sigma_z H = \begin{pmatrix} \mathcal{A} & \mathcal{B} \\ -\mathcal{B}^* & -\mathcal{A}^* \end{pmatrix}, \qquad (6)$$

where $\Sigma_z = \mathrm{diag}(\mathbb{1}, -\mathbb{1}) = [\vec{\alpha}, \vec{\alpha}^\dagger]$ encodes bosonic commutation relations. Note that treating creation and annihilation operators, a_i and $a_i^\dagger$, as separate entities in H and $\mathcal{H}$ shows closed dynamics in particle-hole space. Cavity-mediated corrections to mechanical dissipation ($\gamma_i\kappa/(\Delta^2+\kappa^2) \ll 1$)[43] will be neglected. The rotating (scaled) source terms $\vec{\alpha}_{\mathrm{in}} = (a_{\mathrm{in}}, a_{\mathrm{in}}^\dagger)^T$ represent baths with Bose occupations $\bar{n}_i \approx k_{\mathrm{B}}T/\omega_i$. These fulfil the same Markovian correlations as their lab-frame counterparts, i.e. $\langle \vec{\alpha}_{\mathrm{in}}(t)\vec{\alpha}_{\mathrm{in}}^\dagger(t')\rangle = \mathcal{D}\delta(t-t')$ with diffusion matrix $\mathcal{D} = \mathrm{diag}(\gamma_1(\bar{n}_1+1)\cdots, \gamma_1\bar{n}_1\cdots)$.[53]

When squeezing interactions – which inter-convert particles and holes – are absent ($\mathcal{B} = 0$), the dynamics of a_i and $a_i^\dagger$ are independent, and simply governed by the Hermitian matrices $\mathcal{A}$ and $-\mathcal{A}^*$ respectively. On top of this, if $\Gamma = \gamma\mathbb{1}$, the dynamics can be simply mapped to the closed system via a rigid displacement of the imaginary parts of eigenvalues by $\gamma/2$. This displacement is equivalent to a dynamically-offset basis transformation $\bar{\alpha}'(t) = e^{\frac{\gamma}{2}t}\vec{\alpha}(t)$, relating solutions of ideal and dissipative harmonic oscillators.[54] Therefore, whenever $\mathcal{B} = 0$ is zero, we say that the mechanical modes undergo *Hermitian* dynamics. However, even for $\Gamma = 0$, $\mathcal{M}$ and $\mathcal{H}$ are non-Hermitian if squeezing is present ($\mathcal{B} \neq 0$). We state mechanical modes thus manifest *non-Hermitian dynamics* in that case.

The time evolution of the mechanical amplitudes $\vec{\alpha}'(t)$ can be expressed in terms of the spectral decomposition of $\mathcal{H}$ (Supplementary Information sec. IC). A non-Hermitian $\mathcal{H}$ can host eigenvectors with complex eigenfrequencies ϵ. The different character of eigenfrequencies or *dynamical phases* in parameter space links to generalised parity-time ($G\mathcal{PT}$) symmetries of $\mathcal{H}$ and the associated eigenvectors fulfilling or spontaneously breaking the symmetry.[26] For example, purely oscillatory eigenmodes (real eigenfrequencies) indicate a stable phase (eigenvectors fulfil $G\mathcal{PT}$ symmetry), while positive imaginary eigenfrequencies indicate an unstable phase (eigenvectors break $G\mathcal{PT}$ symmetry). We note that $G\mathcal{PT}$ symmetry coexists with other built-in symmetries of $\mathcal{H}$ that reflect a_i-$a_i^\dagger$ splitting redundancies and must be always fulfilled by eigenvectors (Supplementary Information Sec. IC).

For homogeneous dissipation ($\gamma_i = \gamma$), the symmetries of the open-system dynamical matrix $\mathcal{M}$ are trivially related to those of $\mathcal{H}$, since $\mathcal{M} \mapsto \mathcal{H}$ in the dynamically offset basis $\vec{\alpha}'(t)$. The symmetry classification of $\mathcal{H}$ thus offers insight on dynamical phases, eigensurface topology and symmetry breaking in the open-system. As an example, $\mathcal{PT}$ symmetry in $\mathcal{H}$[55,56] corresponds to 'quasi' or 'passive' $\mathcal{PT}$ symmetry in $\mathcal{M}$.[24,57,58] Similar dynamical mode offsets are also of service in the generalisation to non-symmetric cases (Supplementary Information Sec. IIC).

In our systems, a dynamical phase transition (i.e. spontaneous symmetry breaking) is often accompanied by an EP,[38,59] where eigenvalues and eigenvectors simultaneously coalesce and $\mathcal{H}$ is non-diagonalisable. Alternatively, eigenvalues can split off the real axis without diagonalisability loss[26]. Coalescences are analysed in the studied systems by analytical diagonalisation (see Supplementary Information sec. II B,C,D,E). Defective eigenvector subspaces of $\mathcal{H}$ can also be detected by large numerical values of the condition number for the

inverse of the eigenvector matrix.[60]

Graph representation of quadratic bosonic Hamiltonians and quadrature-independent transport

The existence of a nontrivial gauge field is equivalent to the breaking of time-reversal symmetry (i.e. under the operation $\mathcal{T}$), which signifies the Hamiltonian matrix H can not be rendered real ($H \neq H^*$) via $U(1)$ gauge transformations. This statement is equivalent to having a gauge-invariant synthetic flux in the system.[61] We introduce a powerful graphical representation for the Hamiltonian in Eq. (5) in the main text, revealing loops and nontrivial $U(1)$ synthetic fluxes in particle-hole (Bogoliubov) space. Our graphical framework avoids self-loops in the dynamical matrix representation, previously introduced to describe on-site parametric gain.[62] We consider $\mathcal{A}$ and $\mathcal{A}^*$ as the adjacency matrices for network graphs $\mathcal{G}_a$ and $\mathcal{G}_{a^\dagger}$, disposed in two layers, where nodes correspond to a_i and $a_i^\dagger$ operators respectively (Extended Data Fig. 3).

In this representation, particle-conserving systems ($\mathcal{B} = 0$, Hermitian Eq. (6)) feature disjoint network layers, while parametric gain ($\mathcal{B} \neq 0$, non-Hermitian Eq. (6)) introduces links between $\mathcal{G}_a$ and $\mathcal{G}_{a^\dagger}$ through $\mathcal{B}$ and back via $\mathcal{B}^*$. We note that graph representations for the Hamiltonian and the BdG matrices are similar, as they allow recognising loops in particle-hole space with geometrical phases differing by π. Namely, $\mathcal{H}$ graphs contain layers with adjacency matrices $\mathcal{A}$ and $-\mathcal{A}^*$, connected with each other through $\mathcal{B}$ and $-\mathcal{B}^*$.

This graph representation gives insight into general features of energy transport. In particular, quadrature-independent excitation dynamics is found in networks that feature *disjoint* graphs (e.g. loops), which do not contain direct or indirect links between particles a_i and their corresponding holes $a_i^\dagger$ (Fig. 4). This sublattice symmetry implies pairs of uncoupled blocks in $\mathcal{H}$, which govern the nodes $\vec{\alpha}_L = (a_i, \cdots, a_j^\dagger)$ and $\vec{\alpha}_L^\dagger$ in (independent) graphs L, L^*. For M disjoint graph pairs, the permutation of the modes $\vec{\alpha}$ into each of the graphs, $\vec{\alpha} \mapsto \Pi\vec{\alpha} = (\vec{\alpha}_{L_1}, \vec{\alpha}_{L_1}^\dagger, \ldots, \vec{\alpha}_{L_M}, \vec{\alpha}_{L_M}^\dagger)^T$, block-diagonalises $\mathcal{H}$:

$$\mathcal{H} \mapsto \mathcal{H}' = \Pi\mathcal{H}\Pi = \mathrm{diag}(\mathcal{L}_1, -\mathcal{L}_1^*, \cdots, \mathcal{L}_M, -\mathcal{L}_M^*). \quad (7)$$

Due to charge conjugation symmetry $\mathcal{C}$, particle-hole loops come in pairs. If such loops are disjoint, their associated dynamical matrices $\mathcal{L}_m, -\mathcal{L}_m^*$ ($m = 1, \cdots, M$), will never mix particles and their corresponding hole excitations as they propagate through the graphs. In a single loop pair (Fig 4), dropping the index m,

$$\vec{n}(t) = e^{i\mathcal{L}^* t}\vec{n}(0)e^{-i\mathcal{L}t}, \qquad n_i = a_i^\dagger a_i, \quad (8)$$

having formally integrated $i\partial_t\vec{\alpha}_L = \mathcal{L}\vec{\alpha}_L$ and $i\partial_t\vec{\alpha}_L^\dagger = -\mathcal{L}^*\vec{\alpha}_L^\dagger$, i.e. employing conjugated blocks. Population dynamics in Eq. (8) are independent of the relative phases between $a_i(0)$ and $a_i^\dagger(0)$, i.e. the resonator i quadrature.

Non-Hermitian Aharonov-Bohm effect

The SD shown in Fig. 2 presents the minimal instance of a plaquette in particle-hole space permeated by a nontrivial flux, and illustrates the contrast between the Hermitian and non-Hermitian Aharonov-Bohm (AB) effects. Here we describe how the latter is manifested in the flux-dependent coupling of gainy/lossy quadratures, while we focus on effects in the complex "energy" eigenbasis in Supplementary Information secs. ID, IIB.

The combination of particle-hole conversions with a geometrical AB phase along two superimposed loops L and L^* leads to a redistribution of gain and squeezing in the dimer hybrid quadratures. We choose the gauge $\theta_i = \pi/2$, for which the local resonator quadratures $X_i = (a_i + a_i^\dagger)/\sqrt{2}$ ($Y_i = i(a_i^\dagger - a_i)/\sqrt{2}$) experience loss (gain) in the beam-splitter-uncoupled limit ($J = 0$). The flux in this gauge reads $\Phi = 2\varphi_{12}$. Quadrature interactions can be decomposed in terms of particle-hole conversions along the two loops, i.e. $\mathcal{H}_{\mathrm{SD}} = \mathcal{H}_{\mathrm{SD}}^L + \mathcal{H}_{\mathrm{SD}}^{L^*}$ (loop order $\{a_1, a_2, a_2^\dagger, a_1^\dagger\}$), with

$$\mathcal{H}_{\mathrm{SD}}^L = \begin{pmatrix} 0 & \bar{J} & 0 & 0 \\ 0 & 0 & -i\eta & 0 \\ 0 & 0 & 0 & -\bar{J} \\ -i\eta & 0 & 0 & 0 \end{pmatrix}, \quad \mathcal{H}_{\mathrm{SD}}^{L^*} = (\Sigma_z\mathcal{H}_{\mathrm{SD}}^L\Sigma_z)^\dagger, \quad (9a)$$

where $\bar{J} = Je^{-\frac{i\Phi}{2}}$. $\mathcal{H}_{\mathrm{SD}}^L$ and $\mathcal{H}_{\mathrm{SD}}^{L^*}$ reflect clockwise and counterclockwise propagation of excitations.

The dynamical matrix $\mathcal{H}_{\mathrm{SD}}^{XY} = Q^\dagger\mathcal{H}_{\mathrm{SD}}^L Q + Q^\dagger\mathcal{H}_{\mathrm{SD}}^{L^*}Q$ is obtained by applying the mapping to the quadrature basis Q (order $\{X_1, X_2, Y_1, Y_2\}$):

$$\mathcal{H}_{\mathrm{SD}}^{XY} = \begin{pmatrix} -i\eta & -iJ_\parallel & 0 & iJ_\perp \\ iJ_\parallel & -i\eta & iJ_\perp & 0 \\ 0 & -iJ_\perp & i\eta & -iJ_\parallel \\ -iJ_\perp & 0 & iJ_\parallel & i\eta \end{pmatrix}, \quad (10)$$

The combination of clockwise and counter-clockwise processes with nontrivial Peierls phases then leads to the flux-dependent couplings $J_\parallel = J\sin(\Phi/2)$ and $J_\perp = J\cos(\Phi/2)$ between quadratures.

Gain-loss bases and effective $\mathcal{PT}$ symmetries

Adequate bases for the SD and the SCT can be determined for which one easily recognises an inversion plane separating gain and loss at either side, and therefore potentially a $\mathcal{PT}$ symmetry. For the SD, such symmetry is found using the local quadratures $\vec{R}_{\mathrm{SD}} = (X_1, Y_2, X_2, Y_1)^T$. In a $\theta_i = \pi/2$ gauge, Eq. (10) is block-diagonal for $\Phi = 0$ and reads $\mathcal{H}_{\mathrm{SD}}^{XY} = \mathrm{diag}(\mathcal{H}^{X_1,Y_2}, \mathcal{H}^{X_2,Y_1})$ with the blocks

$$\mathcal{H}^{X_1,Y_2} = i\begin{pmatrix} -\eta & J \\ -J & \eta \end{pmatrix} = \mathcal{H}^{X_2,Y_1}. \quad (11a)$$

governing the dynamics of the independent "quadrature dimers" X_1Y_2 and X_2Y_1. Their closed-system equations of motion read $\dot{\vec{R}}_{\mathrm{SD}} = -i\mathcal{H}_{\mathrm{SD}}^{XY}\vec{R}_{\mathrm{SD}}$.

Each of the blocks Eq. (11a) is $\mathcal{P}_{X_iY_j}\mathcal{T}$-symmetric, with parity operation $\mathcal{P}_{X_iY_j}: X_i \leftrightarrow Y_j$ and $\mathcal{T}$ equivalent to complex conjugation: $i \mapsto -i$. The eigenfrequencies for each block Eq. (11a), namely $\epsilon^{X_iY_j} = \pm\sqrt{J^2-\eta^2}$, are real within the $\mathcal{P}_{X_iY_j}\mathcal{T}$-symmetric region $J > \eta$, in which the corresponding eigenstates respect the symmetry of the dynamical matrix. This is no longer true if $J \leq \eta$, where $\mathcal{P}_{X_iY_j}\mathcal{T}$ is spontaneously broken, with a second order EP at $J = \eta$ indicating the transition.

The recognition of this $\mathcal{PT}$ symmetry allows explaining why non-zero fluxes imply complex, non-real eigenvalues and the disappearance of the EP: they induce coupling between the sub-blocks Eq. (11a) and the *explicit* breaking of $\mathcal{P}_{X_iY_j}\mathcal{T}$ symmetry. This dynamical phase transition along $\Phi \geq 0$ from real to complex eigenvalues can equivalently be characterised in terms of *spontaneous* $G\mathcal{PT}$ symmetry breaking without loss of diagonalisability.[26] An extended theoretical analysis shows that asymmetries in SD shift negligibly the location of degeneracies in the experiment, and lead in general to the expansion of EPs into contours in parameter space (Supplementary Information, sec. IIC).

Similarly, the dynamical phases of the SCT can be classified by $G\mathcal{PT}$ symmetries. The maximum degree of symmetry and degeneracy order corresponds to equal dissipation rates ($\gamma_i = \gamma$). In experiment, we match dissipation rates by applying feedback control. The SCT's dynamics can be integrated, recognising dynamical phase transitions, via a single block of $\mathcal{H}'$ (Eq. (7)): The block acting on $\{a_1, a_2, a_3^\dagger\}$ (gauge $\theta_{23} = \theta_{13} = 0$, where the flux simply reads $\Phi = \varphi_{12}$),

$$\mathcal{L} = \begin{pmatrix} 0 & Je^{-i\Phi} & \eta \\ Je^{i\Phi} & 0 & \eta \\ -\eta & -\eta & 0 \end{pmatrix}. \tag{12}$$

A $G\mathcal{PT}$ symmetry is straightforwardly recognised by switching to the eigenbasis of Eq. (12) for vanishing beam-splitter coupling ($J = 0$), via the unitary transformation

$$U_{gl} = \frac{1}{\sqrt{2}} \begin{pmatrix} \frac{i}{\sqrt{2}} & -\frac{i}{\sqrt{2}} & -1 \\ \frac{i}{\sqrt{2}} & -\frac{i}{\sqrt{2}} & 1 \\ 1 & 1 & 0 \end{pmatrix}. \tag{13}$$

The corresponding eigenmodes $U_{gl}\vec{\alpha}$ are denoted as $a_l = (a_3^\dagger + ia_+)/\sqrt{2}$ (where $a_+ = (a_1 + a_2)/\sqrt{2}$ is the symmetric superposition of resonator 1 and 2 states), $a_g = (a_3^\dagger - ia_+)/\sqrt{2}$, and $a_- = (a_2 - a_1)/\sqrt{2}$. Adopting the order $\{a_l, a_g, a_-\}$, the transformed matrix $\mathcal{L}_{gl} = U_{gl}^\dagger \mathcal{L} U_{gl} = \Xi + \Theta$ splits into a gain/loss contribution

$$\Xi \equiv U_{gl}^\dagger \mathcal{L} U_{gl}|_{J=0} = \mathrm{diag}(-i\sqrt{2}\eta, i\sqrt{2}\eta, 0), \tag{14}$$

and an interactions/frequency shifts contribution

$$\Theta = \begin{pmatrix} \frac{1}{2}J\cos(\Phi) & -\frac{1}{2}J\cos(\Phi) & \frac{J\sin(\Phi)}{\sqrt{2}} \\ -\frac{1}{2}J\cos(\Phi) & \frac{1}{2}J\cos(\Phi) & \frac{J\sin(\Phi)}{\sqrt{2}} \\ -\frac{J\sin(\Phi)}{\sqrt{2}} & \frac{J\sin(\Phi)}{\sqrt{2}} & -J\cos(\Phi) \end{pmatrix}. \tag{15}$$

Equation 13 regroups gain and loss into effective sites a_l, a_- and a_g, revealing an effective gain-loss mirror plane with parity operation $\mathcal{P}_{gl}: a_g \leftrightarrow a_l$.

$\mathcal{L}_{gl}$ respects $\mathcal{P}_{gl}\mathcal{T}$ symmetry for arbitrary flux, where $\mathcal{T}: i \mapsto -i, \Phi \mapsto -\Phi$. The coupling topology, however, is flux-dependent (main text). In particular, when $\Phi = 0$, the dynamical matrix reads

$$\mathcal{L}_{gl}|_{\Phi=0} = \begin{pmatrix} \frac{J}{2} - i\sqrt{2}\eta & -\frac{J}{2} & 0 \\ -\frac{J}{2} & \frac{J}{2} + i\sqrt{2}\eta & 0 \\ 0 & 0 & -J \end{pmatrix}, \tag{16a}$$

i.e. it leaves the mode a_- uncoupled from the remaining $\mathcal{P}_{gl}\mathcal{T}$-symmetric dimer for a_g and a_l (see inset in Fig. 4d). Conversely, a linear trimer structure follows at $\Phi = \pm\pi/2$, where the dynamical matrix reads

$$\mathcal{L}_{gl}|_{\Phi=\pm\pi/2} = \begin{pmatrix} -i\sqrt{2}\eta & 0 & \mp\frac{J}{\sqrt{2}} \\ 0 & i\sqrt{2}\eta & \pm\frac{J}{\sqrt{2}} \\ \mp\frac{J}{\sqrt{2}} & \pm\frac{J}{\sqrt{2}} & 0 \end{pmatrix}. \tag{16b}$$

From Eq. (16a) and Eq. (16b), we can directly observe that flux affects the nature of the arising EPs, which can be either second or third order. Note that while finite synthetic fluxes retain $\mathcal{P}_{gl}\mathcal{T}$ symmetry of $\mathcal{L}$, they break the mirror symmetry $\mathcal{P}_{12}: a_1 \leftrightarrow a_2$, affecting the localisation transition above the EP (see main text, Extended Data Fig. 4). The full expressions for the eigenspectra and population dynamics that illustrate this behaviour can be found in the Supplementary Information Sec. IID,E.

Subdominant and non-Lorentzian spectral features in the squeezing dimer

In the thermomechanical noise spectra of the SD in Fig.2e,f, we expect narrow and broad, frequency-degenerate, resonances. We show this in the ideal SD ($\gamma_i = \gamma$), whose spectrum is obtained in a closed form using the relationship via the quantum regression theorem (Supplementary Information IE)

$$\mathcal{S}(\omega) = \langle \vec{\alpha}^\dagger(\omega)\vec{\alpha}(\omega)\rangle = \chi_m^\dagger(\omega)\mathcal{D}\chi_m(\omega), \tag{17}$$

with mechanical susceptibility matrix $\chi_m(\omega) = i/(\omega\mathbb{1} - \mathcal{H}_{\mathrm{SD}})$ and diffusion matrix $\mathcal{D}$, given earlier. The noise spectrum of resonator $i \in (1, 2)$ is given by the diagonal element $\mathcal{S}_{ii}(\omega)$. An explicit calculation for the SD shows that even in the simplified limit of equal resonator bath occupations $\bar{n}_i = \bar{n}$, the spectrum consists of 4 superimposed Lorentzian responses located at the real parts of the eigenfrequencies of $\mathcal{H}_{\mathrm{SD}}$ for $\Phi = \pi$, where two pairs of resonances split by $2J$ and

$$\mathcal{S}_{ii}(\omega) \propto \gamma \sum_{\Omega=\pm J} \left(\frac{\bar{n}+1}{(\gamma+2\eta)^2 + 4(\omega-\Omega)^2} + \frac{\bar{n}}{(\gamma-2\eta)^2 + 4(\omega-\Omega)^2} \right). \tag{18}$$

From Eq. (18), it is apparent that the spectral weight in the rotating frame at $\pm J$ in the stable regime ($\gamma > 2\eta$) is concentrated in a dominant, narrow resonance with linewidth $\gamma - 2\eta$, on top of an additional, heavily damped contribution with linewidth $\gamma + 2\eta$.

In contrast, the branch-cut topology mandated by the EP at $\Phi = 0$ results in a non-Lorentzian thermal response. If $\Phi = 0$, the spectrum contains non-Lorentzian contributions

$$\mathcal{S}_{ii}(\omega) \propto \frac{2\gamma\left[(2\bar{n}+1)\left(\gamma^2+4\left(\eta^2+J^2+\omega^2\right)\right)-4\gamma\eta\right]}{d(\omega)},$$
$$d(\omega) = 8\omega^2\left(\gamma^2+4\left(\eta^2-J^2\right)\right) + \left(\gamma^2-4\left(\eta^2-J^2\right)\right)^2+16\omega^4. \quad (19a)$$

Equation 19a reduces at the EP ($J = \eta$) to the expression which shows directly a double-Lorentzian response:[63]

$$\mathcal{S}_{ii}(\omega) \propto \frac{\gamma}{2}\frac{(2\bar{n}+1)\left(2J^2+\gamma^2/4+\omega^2\right)-\gamma J}{\left(\gamma^2/4+\omega^2\right)^2}. \quad (19b)$$

This functional form implies deviations in the experimental linewidths in the vicinity of an EP obtained from Lorentzian spectral fitting (Extended Data Fig. 2 and Supplementary Information sec. IIIA).

Design and fabrication

The device, shown in Extended Data Fig. 5a, was designed as a sliced photonic crystal nanobeam with two beam halves of different mass to create non-degenerate mechanical modes. The cavity was defined away from the beams' centres to optically access flexural modes with even as well as odd symmetries. The cavity is designed as a single-site defect, by locally varying hole pitch in the one-dimensional photonic crystal. This creates a cavity with significant optical coupling to light normally incident from free space.[64] It also results in a relatively large optical linewidth ($\kappa \approx 320$ GHz), ensuring that the cavity responds linearly to thermal excitations (at the optimal detuning), such that nonlinear transduction[65] and detrimental reduction of the optical spring shift are insignificant. Devices were fabricated from a silicon-on-insulator substrate, with a 220 nm device layer and 3 µm buried oxide layer (BOX). A 50 nm layer of diluted hydrogen silsesquioxane resist (1:2 in methyl isobutyl ketone) was spin-coated, and electron-beam lithography (Raith Voyager) was used to write patterns on the sample. After developing in tetramethylammonium hydroxide, an anisotropic etch of the exposed device layer was done using inductively coupled plasma–reactive ion etching with HBr and O_2 gases. The nanobeams were suspended in a wet etch of the underlying BOX layer with hydrofluoric acid followed by critical point drying.

Experimental setup

A schematic of the experimental setup is presented in Extended Data Fig. 5b. The sample was placed, with the devices rotated by 45° relative to the vertical polarisation of the incoming light, in a vacuum chamber at room temperature at a pressure of $\sim 2 \times 10^{-6}$ mbar. A tunable laser (Toptica CTL 1500) connected through a Thorlabs LN81S-FC intensity modulator (IM) was used as the drive laser (power incident on device $P_{\mathrm{drive}} = 1.0$ mW). A small part of the modulated drive laser light was split using a fibre-based beam splitter and fed onto a fibre-coupled fast photodetector (New Focus 1811, DC-coupled) to monitor the drive signal. A second laser (New Focus TLB-6328 or Toptica CTL 1550) far detuned from the cavity resonance ($\omega_{\mathrm{det}} - \omega_c \approx -2.5\kappa$) was used as the detection laser (power incident on device $P_{\mathrm{det}} = 2 - 4$ mW). The lasers were combined on a fibre-based beam combiner and launched using a fibre collimator into the free-space setup.

Control signals were generated by a Zurich Instruments UHFLI lock-in amplifier. One output of the lock-in amplifier carried signals to generate interactions, while the other output carried coherent excitation signals. Both outputs were routed through individual radio-frequency (RF) switches (Mini-Circuits ZYSWA-2-50DR+), combined, amplified (Mini-Circuits ZHL-32A+ with 9 dB attenuation) and connected to the RF port of the IM to drive and modulate the nanobeam mechanics. For time-resolved experiments, a synchronised two-channel signal generator (Siglent SDG1062X) was used to generate pulses to actuate both RF switches and trigger the lock-in amplifier acquisition.

Reflected detection laser light that interacted with the cavity was filtered using a cross-polarised detection scheme, fibre coupled, separated from the drive laser using a tunable bandpass filter (DiCon), and detected on a fast, low-noise photodetector (New Focus 1811, AC-coupled). Intensity modulations of the detection laser encoding resonator displacements were analysed using the lock-in amplifier.

To generate a feedback signal, the electronic displacement signal was split and filtered using a digital signal processor (DSP, RedPitaya STEMlab 125-14) that implemented a configurable electronic bandpass filter with tunable gain and phase shift (using the PyRPL suite). The output of the DSP was combined with the control signals just before the RF amplifier.

Experimental procedure

Resonator characterisation

The intrinsic, optically unmodified resonator frequencies $\tilde{\omega}_i$ and linewidths $\tilde{\gamma}_i$ were obtained by switching off the drive laser and recording a thermomechanical spectrum with the detection laser. A power sweep of the detection laser verified that the detection laser did not induce a noticeable optical shift in

frequency or linewidth. The vacuum optomechanical coupling for the resonators $g_0^{(i)}$ is estimated from nonlinear transduction,[65] with fitted values $g_0^{(i)}/(2\pi) = \{5.30 \pm 0.14, 5.86 \pm 0.17, 3.29 \pm 0.30, 3.12 \pm 0.89\}$ MHz for the four resonators, respectively. The linewidth of the optical cavity was estimated from the detuning dependence of the spring shift (Extended Data Fig. 6).

To compensate for variations in incoupling and outcoupling efficiency, caused by position drift of the sample stage, the following reference procedure was performed immediately before every experiment: A thermomechanical spectrum was taken to obtain the spring-shifted resonator frequencies ω_i, linewidths γ_i, and root-mean-square (rms) displacement voltage levels $z_{\mathrm{rms},i}$. From the rms level, the displacement voltage corresponding to a single phonon was calculated using $z_{\mathrm{ph},i}^2 = z_{\mathrm{rms},i}^2/\left(\bar{n}_i\tilde{\gamma}_i/\gamma_i\right)$, where $\bar{n}_i = k_B T/\hbar\omega_i$ is the occupation of the resonator's phonon bath at room temperature $T = 295$ K. The ratio $\tilde{\gamma}_i/\gamma_i$ compensates for thermo-optically induced dynamical backaction[66] that changes the effective bath temperatures[29] (see Extended Data Fig. 6d). Control over dynamical backaction is also employed in the SD experiments to equalise loss rates for the two resonators. Fine-tuning the laser intensity allows to match the two linewidths of modes 3 and 4 specifically, as they exhibit different scaling with mean photon number.

Calibration of control signals

To find the linear operation point of the IM, a sinusoidal modulation voltage was applied while sweeping its amplitude and monitoring the modulated drive laser. The IM bias voltage was varied to minimise the variation in DC transmission as a function of modulation amplitude. To compensate for frequency-dependent transmission in the RF chain, the relation between control signal voltage amplitude V_{m} and modulation depth c_{m} was measured individually for every tone using the DC-coupled modulation monitor detector.

For the BST experiments in Fig. 1, a linear relation between modulation amplitude V_{m} and the beamsplitter coupling J_{ij} induced by sinusoidal modulation at $\omega_{\mathrm{m}} = \omega_i - \omega_j$, $i \neq j$ was established by sweeping V_{m}, recording thermomechanical spectra of resonators i and j and fitting the frequency splitting of the hybridized modes.

Spectral estimation of the strength of a squeezing interaction is less precise due to the spectral superposition of gain and loss (see Extended Data Fig. 7). Therefore, in the other experiments, the squeezing and beamsplitter interaction strengths η_{ij}, J_{ij} induced by a sinusoidal drive laser modulation at frequency $\omega_{\mathrm{m}} = \omega_i \pm \omega_j$ (for $i \neq j$ or $i = j$) and modulation depth c_{m} were obtained using the relationship

$$\{\eta_{ij}, J_{ij}\} = c_{\mathrm{m}}\sqrt{\delta\omega_i \delta\omega_j}/2, \tag{20}$$

where $\delta\omega_i = \omega_i - \tilde{\omega}_i$ is the optical spring shift of resonator i. Note that $\delta\omega_i$ and $\delta\omega_j$ always have the same sign. Using this relation avoids the need to know the photon-phonon coupling rates $g_0^{(i)}$ and cavity incoupling efficiency precisely. To verify, the effective beam-splitter interaction strength obtained above was compared to the frequency splitting observed in thermomechanical spectra for a sweep of the modulation depth c_{m} (see Extended Data Fig. 1). From this, a difference between calculated and actual interaction strength of about 10% was obtained, presumably due to a difference in the modulation detector sensitivity at DC or a limited modulation range of the IM. This difference was applied as a correction factor to all calculated interaction strengths.

For the SD experiments (Fig. 2 and 3), performed with high modulation depths $c_{\mathrm{m}} > 0.5$, a relation between c_m and V_m was established using the first order Bessel function $J_1(x)$, derived from a Jacobi-Anger expansion of the IM cosine response. In addition, a linear correction on the scaling of the beam-splitter coupling J was obtained by fitting the linear frequency splitting for $\Phi = \pi$ (as shown in Fig. 3b) as a function of c_{m}.

In the BST experiments, the flux offset $\Phi_0 = \varphi_{23} + \varphi_{31}$ was obtained by extracting eigenfrequencies from thermomechanical spectra as a function of φ_{12} and fitting those to the eigenfrequencies $\epsilon_k = 2J\cos((2\pi k + \Phi)/3)$ of the Hamiltonian H_{BST} in Eq. (1) indexed by $k = \{-1, 0, 1\}$, where $\Phi = \Phi_0 + \varphi_{12}$. In the other experiments, to circumvent spectral estimation of the flux and to facilitate the analysis of (anti)squeezed quadratures, the phases of the control tones are referred to an effective time origin internal to the lock-in amplifier, which allows to define a deterministic gauge in which the modulation phases are set and the response is analysed. This method was verified by applying it to the BST and comparing it to the flux offset fitting method outlined above.

To realise the modulation of dissipation rates in the SCT experiments, a feedback signal was obtained by filtering the electronic displacement signal around each resonator's frequency ω_i in parallel (second-order filter half-width at half-maximum 78 kHz), applying individual gains and phase shifts, and digitally combining the filtered signals. For each mode, the optimal feedback phase shift was found by taking thermomechanical spectra using fixed feedback gain for a full sweep of the phase shift, fitting the extracted linewidths with a sinusoidal variation and selecting the shift with the most significant change in linewidth (see Extended Data Fig. 8). Subsequently, for the optimal phase shift, thermomechanical spectra were taken for various settings of the feedback gain and a linear relation was fitted between gain and extracted linewidths.

Analysis of the displacement signal

The electronic displacement signal was demodulated in parallel at each resonator's frequency ω_i using electronic

local oscillators internal to the lock-in amplifier that are referenced to the same time origin as the control tones. For each resonator, the demodulated in-phase (I_i) and quadrature (Q_i) components were filtered (third-order low-pass filter, 3 dB bandwidth 50 kHz) and combined into a complex amplitude $z_i(t) = I_i(t) + iQ_i(t)$ that is formally equivalent to the resonator amplitude in the rotating frame. The complex amplitudes of all resonators involved were acquired simultaneously, at a rate between 50 and 500 kSa/s, depending on the experiment. These complex time traces were normalized using the signal levels obtained in the reference procedure described earlier and were either *i)* analysed directly to yield phase-space distributions; *ii)* averaged coherently, i.e. $\langle z_i(t)\rangle$; or *iii)* Fourier transformed (Hann windowing function), squared and averaged to yield energy spectral densities (ESD). In the last case, the low-pass filter was compensated for by dividing spectral densities by the filter frequency response. Time-resolved experiments were averaged over 1000 runs.

The total signal delay through the setup, from the LIA control outputs via the sample to the LIA input, was determined by driving each of the resonators and measuring the coherent response (see Extended Data Fig. 9). The phase offset α_i between drive tone and coherent response of resonator i was extracted and fitted linearly against the resonator frequencies ω_i. The fitted delay was used to relate the quadratures of the demodulated amplitudes $z_i(t)$ to those defined by the control tones. This relation was verified for resonators 3 and 4 (i.e. the modes that participate in the SD) by turning on a single-mode squeezing interaction, recording a thermomechanical time trace, constructing a phase space distribution and fitting the angle of the squeezed and anti-squeezed principal quadrature axes (see Extended Data Fig. 7).

Error estimation

The error on fitted values like frequencies and linewidths originates from multiple sources. Error bars in plots indicate $\pm 2\sigma$, i.e. a 95% confidence interval for a normal distribution.

The stability of the interaction strength over typical measurement timescales (~ 100 s) is controlled by the stability of the drive laser power (relative standard deviation $\sigma_{P_{\mathrm{drive}}}/P_{\mathrm{drive}} \approx 2\cdot 10^{-3}$) entering Eq. (20) through $\delta\omega_i$ and the stability of the modulation tone amplitude (relative standard deviation $\sigma_{c_{\mathrm{m}}}/c_{\mathrm{m}} \approx 10^{-3}$).

In addition, jitter of the spring shift $\delta\omega_i$ due to variations in drive laser power and incoupling efficiency controls the detuning of the control signals. For resonators with comparable $g_0^{(i)}$ (i.e. resonators 1 & 2 and resonators 3 & 4), the effect of detuning jitter on beam-splitter interactions – which depend only on their frequency difference – is reduced. To estimate the effect of detuning jitter on the effective linewidth change induced by squeezing interactions, a Monte Carlo method is employed.

Finally, the fit uncertainty is estimated using a numerical approximation of the Jacobian matrix.

The standard error of the experimental (co)variances $\sigma(A,B)$ of quadratures A and B is estimated using the statistical relationship $\mathrm{Std}(\sigma(A,B)^2) \approx \sqrt{\frac{1}{n-1}\left(\sigma(A,B)^4 + \sigma(A,A)^2\sigma(B,B)^2\right)}$ where Std denotes the standard deviation. Here, n is the number of thermally independent measurement points, given by $n = T\gamma_i/2$, where $T = 0.3$ s is the duration of the measurement record and γ_i is the dissipation rate of the resonator involved.

[41] Ozawa, T., Price, H. M., Goldman, N., Zilberberg, O. & Carusotto, I. Synthetic dimensions in integrated photonics: From optical isolation to four-dimensional quantum Hall physics. *Phys. Rev. A* **93**, 043827 (2016).

[42] Goldman, N., Budich, J. & Zoller, P. Topological quantum matter with ultracold gases in optical lattices. *Nat. Phys.* **12**, 639–645 (2016).

[43] Reiter, F. & Sørensen, A. S. Effective operator formalism for open quantum systems. *Phys. Rev. A* **85**, 032111 (2012).

[44] Fang, K., Yu, Z. & Fan, S. Realizing effective magnetic field for photons by controlling the phase of dynamic modulation. *Nat. Photonics* **6**, 782–787 (2012).

[45] Mahboob, I., Okamoto, H., Onomitsu, K. & Yamaguchi, H. Two-mode thermal-noise squeezing in an electromechanical resonator. *Phys. Rev. Lett.* **113**, 167203 (2014).

[46] Leuch, A. *et al.* Parametric symmetry breaking in a nonlinear resonator. *Phys. Rev. Lett.* **117**, 214101 (2016).

[47] Calvanese Strinati, M., Bello, L., Pe'er, A. & Dalla Torre, E. G. Theory of coupled parametric oscillators beyond coupled Ising spins. *Phys. Rev. A* **100**, 023835 (2019).

[48] Bello, L., Calvanese Strinati, M., Dalla Torre, E. G. & Pe'er, A. Persistent coherent beating in coupled parametric oscillators. *Phys. Rev. Lett.* **123**, 083901 (2019).

[49] Nonlinear oscillations, dynamical systems, and bifurcations of vector fields. *J. Appl. Mech.* **51**, 947–947 (1984).

[50] Gardiner, C. & Zoller, P. *Quantum noise* (Springer, 2004).

[51] Blaizot, J.-P. & Ripka, G. *Quantum theory of finite systems* (MIT Press, 1986).

[52] Rossignoli, R. & Kowalski, A. M. Complex modes in unstable quadratic bosonic forms. *Phys. Rev. A* **72**, 032101 (2005).

[53] Aranas, E. B., Javed Akram, M., Malz, D. & Monteiro, T. S. Quantum noise spectra for periodically driven cavity optomechanics. *Phys. Rev. A* **96**, 063836 (2017).

[54] Richards, J. A. *Analysis of periodically time-varying systems* (Springer Science & Business Media, 2012).

[55] Bender, C. M. & Boettcher, S. Real spectra in non-Hermitian Hamiltonians having $\mathcal{PT}$ symmetry. *Phys. Rev. Lett.* **80**, 5243 (1998).

[56] Rüter, C. E. *et al.* Observation of parity–time symmetry in optics. *Nat. Phys.* **6**, 192–195 (2010).

[57] Ornigotti, M. & Szameit, A. Quasi $\mathcal{PT}$-symmetry in passive photonic lattices. *J. Opt.* **16**, 065501 (2014).

[58] Li, H., Mekawy, A., Krasnok, A. & Alù, A. Virtual parity-time symmetry. *Phys. Rev. Lett.* **124**, 193901 (2020).

[59] Heiss, W. D. The physics of exceptional points. *J. Phys. A: Math. Theor.* **45**, 444016 (2012).

[60] Moiseyev, N. *Non-Hermitian quantum mechanics* (Cambridge University Press, 2011).

[61] Koch, J., Houck, A. A., Hur, K. L. & Girvin, S. M. Time-reversal symmetry breaking in circuit-QED based photon lattices. *Phys. Rev. A* **82**, 043811 (2010).

[62] Ranzani, L. & Aumentado, J. Graph-based analysis of nonreciprocity in coupled-mode systems. *New J. Phys.* **17**, 023024 (2015).

[63] Takata, K. *et al.* Observing exceptional point degeneracy of radiation with electrically pumped photonic crystal coupled-nanocavity lasers. *Optica* **8**, 184 (2021).

[64] Leijssen, R. & Verhagen, E. Strong optomechanical interactions in a sliced photonic crystal nanobeam. *Sci. Rep.* **5**, 15974 (2015).

[65] Leijssen, R., La Gala, G. R., Freisem, L., Muhonen, J. T. & Verhagen, E. Nonlinear cavity optomechanics with nanomechanical thermal fluctuations. *Nat. Commun.* **8**, 16024 (2017).

[66] Hauer, B. D., Clark, T. J., Kim, P. H., Doolin, C. & Davis, J. P. Dueling dynamical backaction in a cryogenic optomechanical cavity. *Phys. Rev. A* **99**, 053803 (2019).

[67] Frimmer, M. & Novotny, L. The classical Bloch equations. *Am. J. Phys.* **82**, 947–954 (2014).

Acknowledgements

The authors thank Clara Wanjura, Andreas Nunnenkamp, and Matteo Brunelli for useful discussions, and Marc Serra-Garcia, Said Rodriguez, Femius Koenderink, and Oded Zilberberg for critical reading of the manuscript. This work is part of the research programme of the Netherlands Organisation for Scientific Research (NWO). The authors acknowledge support from the the European Research Council (ERC starting grant no. 759644-TOPP) and the European Union's Horizon 2020 research and innovation programme under grant agreement no. 732894 (FET Proactive HOT). J. d. P. acknowledges financial support from the ETH Fellowship program (grant no. 20-2 FEL-66).

Author contributions

J.d.P. developed the theoretical framework. J.S. fabricated the sample, performed the experiments, analysed the data and aided in constructing the theoretical approach. E.V. conceived and supervised the project. All authors contributed to the interpretation of results and writing of the manuscript.

Competing interest declaration

The authors declare no competing interests.

Additional information

Supplementary Information is available for this paper.

Correspondence and requests for materials should be addressed to Ewold Verhagen (verhagen@amolf.nl) or Javier del Pino (jdelpino@phys.ethz.ch).

Data availability

The data in this study are available from the Zenodo repository at [to be inserted].

EXTENDED DATA FIG. 1: Estimation of beam-splitter interaction strengths. a Mode splitting induced by a beam-splitter interaction observed in thermomechanical spectra. Each column corresponds to a beam-splitter interaction induced between a pair of resonators $i \leftrightarrow j$ (left: $1 \leftrightarrow 2$, middle: $2 \leftrightarrow 3$, right: $1 \leftrightarrow 3$) by a single drive laser modulation at frequency $\Delta\omega_{ij} = \omega_i - \omega_j$, where $\omega_{i,j}$ is the frequency of resonator i, j. Thermomechanical spectra (top row: resonator i, bottom row: resonator j) are recorded for increasing modulation depth c_m. The linear relationship $J_\mathrm{est} = c_\mathrm{m}\sqrt{\delta\omega_i\delta\omega_j}/2$ is used to estimate the coupling strength J_est (top axis) from c_m, where $\delta\omega_{i,j}$ is the optical spring shift of mode i, j. The estimated mode splitting (dashed) is slightly larger than observed, presumably due to frequency-dependent transduction (at DC and $\Delta\omega_{ij}$) in the measurement of c_m. The difference is quantified by extracting Lorentzian peak frequencies from the spectra and subsequently fitting those linearly against modulation depth, and results in an observed mode splitting slope that is 78%, 90% and 90% of the estimated slope respectively. The average estimation offset of 86% is applied to all (beam-splitter and squeezing) interaction strength calculations in our experiments. **b** Time evolution of the coherent amplitude (in units of their zero point fluctuations) of a pair of resonators (1, blue and 2, orange) coupled through a beam-splitter interaction (strength $J/(2\pi) = 5$ kHz). Resonator 1 is initially (time $t < 0$) driven to a high amplitude steady state by a coherent drive laser modulation. At $t = 0$, the drive is switched off and the interaction is switched on. Rabi oscillations induced by the coupling interaction are observed, where energy is transferred back and forth between the resonators until the coherent energy in the resonators is dissipated. These dynamics illustrate the possibility for a transfer scheme in the strong coupling regime where couplings are interrupted after a Rabi semi-cycle i.e., a time $t_\pi = \pi/(2J)$. The energy transfer efficiency for this process can be calculated [67] to be $\approx 64\%$ for corresponding parameters and 70% for the coupling rates presented in Fig. 1.

EXTENDED DATA FIG. 2: Frequency and linewidth modulation in the squeezing dimer. a Experimental resonance frequencies (top) and linewidths (bottom) obtained by fitting a superposition of Lorentzian lineshapes to the thermomechanical spectra in Fig. 3c,d. Grey curves indicate theoretical values of $\mathrm{Re}(\epsilon)$ (top) and $\mathrm{Im}(\epsilon)$ (bottom). Two peaks were fitted to the spectra for $\Phi = 0$ (left), as for that flux both eigenvalues are expected to be doubly degenerate for all J. The observed branching of frequencies and linewidths is characteristic of an exceptional point. Four peaks were instead fitted for $\Phi = \pi$ (middle), where the exceptional point behaviour completely vanishes, and spectra are fitted well with a combination of broad and narrow peaks at two frequencies. When varying flux in the rightmost panel, the grey shaded areas depict the regions near $\Phi = 0, \pi$ where a fit of two peaks provided better results than a fit of four. Note that near the exceptional point, the non-Lorentzian nature of the spectrum causes the fitted values of the Lorentzian linewidths to deviate from the theoretical $\mathrm{Im}(\epsilon)$. This origin of the deviation is confirmed by applying the same fit procedure to theoretically predicted spectra (inset, left bottom panel), which shows the same deviation. Error estimation is described in Methods. **b** Thermomechanical spectra for several values of J/η, for $\Phi = 0$ (blue) and $\Phi = \pi$ (red). Solid lines show Lorentzian fits. **c** Similar, for different values of Φ at $J = \eta$.

EXTENDED DATA FIG. 3: Network graph representation of general quadratic Hamiltonians. Schematic of an arbitrary dynamical matrix $\mathcal{H}$, acting on a Nambu-like vector $\vec{\alpha} = (a_1, a_2, \cdots, a_N, a_1^\dagger, a_2^\dagger, \cdots, a_N^\dagger)$. Particle annihilation (hole creation) operators, a_i, are represented by blue nodes, whereas hole annihilation (particle creation) operators are represented by orange nodes. $\mathcal{H}$ includes excitation-conserving interactions (matrix $\mathcal{A}$), which link particle operators (e.g. terms $\mathcal{A}_{ij}a_i^\dagger a_j$) and hole operators (e.g. terms $\mathcal{A}_{ji}^* a_j a_i^\dagger$). Squeezing interactions (with complex amplitude matrix $\mathcal{B}$) contain pairs $\mathcal{B}_{ij}a_i^\dagger a_j^\dagger$ which can be visualized to either annihilate two particles i, j or to annihilate a particle in i an create hole in j, hence the connection between particle and hole networks (green). Mutatis mutandis, terms $\mathcal{B}_{ij}^* a_i a_j$ can be similarly visualized.

EXTENDED DATA FIG. 4: Calculated eigenstates of the loop $a_1, a_2, a_3^\dagger$ in the SCT studied in Fig. 4. **a** Phase diagram for the imaginary part of the eigenfrequencies, showing the stability-to-instability boundary in $\xi - \Phi$ space, where $\xi = J/(2\sqrt{2}\eta)$ and $\gamma_i = 0$. Such boundary is associated with a second order exceptional contour. **b** Cuts of the eigenfrequency Riemann surfaces along $\Phi = 0$, shown as a red dashed trajectory in the phase diagram, as a function of the ratio $\xi = J/(2\sqrt{2}\eta)$. The squared weights of the $J = 0$ eigenstates in the corresponding eigenvectors are shown in the colorscale. The weights are calculated from the symplectic projections (Σ_z product) on the gainy/lossy combinations a_g, a_l and the passive mode a_-. A second order exceptional point (denoted EP2), found for $J = 2\sqrt{2}\eta$, is highlighted. As $J < 2\sqrt{2}\eta$, $\mathcal{P}_{gl}\mathcal{T}$ symmetry is spontaneously broken, inducing eigenstate localisation. The antisymmetric 1-2 mode a_- is detached from this mechanism and remains uncoupled. Real and imaginary parts are re-scaled by η. **c** Similar data along the cut $\Phi = \pi/2$ (corresponding to the blue dashed line in **a**, which shows the third-order exceptional point (EP3, at $J = \sqrt{2}\eta$). The $\mathcal{P}_{gl}\mathcal{T}$ symmetry broken states are now hybrid combinations of a_g, a_- and a_l, a_- modes. Such combinations break $\mathcal{P}_{12}\mathcal{T}$ symmetry as well, as explained in the main text.

EXTENDED DATA FIG. 5: Experimental setup. **a** Electron micrograph (left; tilt 45°, inset; top view) showing a device as used in our experiments. In the top silicon device layer (thickness 220 nm), three suspended beams are defined with teeth separated by a narrow slit ($\sim$ 50 nm). Between each outer beam and the central beam, a photonic crystal cavity is defined that hosts an optical mode (right; simulated electric field y-component E_y). The mode's energy is strongly confined to the narrow slits, inducing large parametric interaction with flexural mechanical resonances of the two beams. The cavity's off-centre position ensures coupling to both even and odd resonances. In the presented experiments, we only use one of the two cavities. The widths of the outer beams' straight sections are intentionally made unequal, such that the mechanical resonances of all beams are detuned. The top layer is supported by pedestals etched out in the buried silicon oxide layer. **b** Schematic of the experimental set-up. IM, intensity modulator; LP, linear polariser; PBS, polarising beamsplitter; BPF, optical bandpass filter; PD1, PD2, photodiode; DSP, digital signal processor; SWs, microwave switches; LIA, ultrahigh-frequency lock-in amplifier; SG, signal generator. The LIA ports serve to (Out) drive the IM through an amplification stage (not shown) and to (In) analyse intensity modulations of the drive laser (for calibration) and detection laser. For time-resolved measurements, the SG is programmed to (Out) actuate the drive signal switches and trigger the LIA acquisition. The DSP optionally generates a feedback signal to modify resonator damping rates.

EXTENDED DATA FIG. 6: Optical spring shift and opto-thermal backaction. **a** Thermomechanical noise spectra of the first few mechanical modes imprinted on an unmodulated single drive/detection laser, as the laser's frequency (ω_L) is swept across the cavity resonance. The four most intense peaks around frequencies $\omega_i/(2\pi) \approx \{3.7, 5.3, 12.8, 17.6\}$ MHz correspond to flexural modes (labelled i) of the individual beam halves and show frequency tuning characteristic to the optical spring effect, while the other modes represent non-linearly transduced harmonics of those modes. **b** Zoomed-in thermomechanical noise spectra of the first three resonators. **c** From the spectra in **b**, resonance frequencies ω_i (blue circles) and linewidths γ_i (orange circles) are extracted. The resonance frequencies are fitted using the standard optical spring model (solid blue). Across all resonators, we find agreement in the fitted cavity resonance $\omega_c/(2\pi) = 195.62$ THz and linewidth $\kappa/(2\pi) = 320$ GHz (Q factor $Q \approx 600$). The small sideband resolution $\omega_i/\kappa \approx 10^{-5}$ suggests very little change in linewidth due to dynamical cavity backaction (dashed orange). The linewidth modulations we observe suggest the presence of an opto-thermal retardation effect.[66] Displayed errors correspond to fit uncertainty, smaller than symbol size on the fitted frequencies (Methods). **d** Drive laser frequency sweep while now using a separate, fixed frequency, far-detuned detection laser. The fixed transduction of mechanical motion onto this detection laser allows a comparison of resonance peak area $A_i(\omega_L)$, versus linewidth $\gamma_i(\omega_L)$ as the drive laser frequency ω_L is varied. The resonance peak area of mode i is proportional to the variance $\langle X_i^2 \rangle$ of its displacement X_i, which is proportional to its temperature T_i. Dynamical backaction modifies the effective mode temperature through $T_i = T_0\,(\tilde{\gamma}_i/\gamma_i)$[29], where T_0 is the initial temperature and $\tilde{\gamma}_i$ is the mode's intrinsic linewidth, determined by switching off the drive laser. Our data is well explained by linear fits of $A_i(\omega_L)$ versus $\tilde{\gamma}_i/\gamma_i(\omega_L)$ (dashed), confirming the effective temperature model.

EXTENDED DATA FIG. 7: Single-mode squeezing and linewidth modulation by parametric driving. **a** Parametric gain induced by a single-mode squeezing interaction observed in thermomechanical spectra. Each row corresponds to a separate experiment where resonator i (1 through 4) is subjected to a single-mode squeezing interaction of strength η. As η is increased, the resonance transitions from the broad intrinsic linewidth to a narrow parametric resonance. **b** The phase-space distribution of the thermal fluctuations of resonator i (left: 3, right: 4) subject to a single-mode squeezing interaction of strength $\eta/(2\pi) = 1$ kHz with squeezing angle $\theta = \pi/2$ reveals a squeezed thermal state. The squeezed (antisqueezed) quadrature X (Y), measured in units of the thermal equilibrium amplitude $\sqrt{\bar{n}_i}$, are referenced using the propagation delay (Methods). **c** Fitted Lorentzian full-width at half-maximum linewidths of the resonances show in a). Even though a superposition of two degenerate resonances is expected – a broadened resonance of the antisqueezed quadrature and a narrowed resonance of the squeezed quadrature – only a single one can be successfully fitted in each spectrum. This reflects the fact that the highly populated narrowed resonance dominates the broadened resonance. As the parametric gain η is increased, each resonator's squeezed quadrature linewidth is expected to decrease by $\Delta\gamma = -2\eta$ (dashed lines), until parametric threshold is reached at $\eta = \gamma_i/2$, where γ_i is the intrinsic linewidth of resonator i. The fitted linewidths follow the expected trend quite closely for intermediate η, while for lower η the narrow resonance is presumably not yet fully dominant and for larger η high-amplitude non-linear effects are prominent. Error bars correspond to fit uncertainty, and are smaller than symbol size in most points (Methods).

EXTENDED DATA FIG. 8: Damping rate adjustment by feedback. Resonator thermomechanical spectra (top row) and fitted full-width half-maximum linewidths (bottom row) adjusted by feeding back electronically filtered and phase-shifted resonator displacement signals onto the drive laser modulation (left two columns, resonator 1; right two columns, resonator 2). The resonator linewidth (circles) and frequency shift (crosses) vary sinusoidally with the feedback phase ϕ_{fb} (odd columns). By fitting the linewidth variation (solid black), the optimal phase shift to increase the damping rate is selected. The frequency variation (dashed grey) expected from the fitted linewidth modulation, relative to the resonator frequency with feedback off (dashed orange), lags by $\pi/2$ radians. For the optimal feedback phase shift, an increase in linewidth is observed for increasing gain G, while the resonator frequency remains unaffected (even columns). The slope of the linear fit (solid black) can be used when setting a resonator's linewidth to a desired value. Error bars reflect fit uncertainty and control parameter stability, and are typically smaller than symbol size (Methods).

EXTENDED DATA FIG. 9: Resonator coherent response. a Amplitude $|a_i|$ (blue, left axis) and phase ϕ_i (orange, right axis) of the complex response $a_i(\Delta) = e^{i(\phi_i(\Delta)+\alpha_i)}|a_i(\Delta)|$ of resonators 1 through 4 (resonance frequencies ω_i) to a drive laser modulation at a frequency ω_d close to resonance (drive detuning $\Delta = \omega_d - \omega_i$). α_i is the phase offset due to signal delay through the set-up. A Lorentzian response $a_i = e^{i\alpha_i} A_i \frac{\gamma_i/2}{i\gamma_i/2-\Delta}$ is fitted to the data (dashed). Error bars in panel (a) reflect the spread in repeated measurement while the error bars in (b) correspond to fit uncertainty and are smaller than the symbol size (Methods). **b** Phase offset α_i versus resonance frequency $\omega_i/(2\pi)$. A linear fit (dashed) of $\alpha_i = -\omega_i\tau$ implies a signal delay $\tau = 106.7$ ns.

EXTENDED DATA FIG. 10: Tunable single-mode and effective two-mode squeezing in the squeezing dimer. a Intra-resonator squeezing as a function of the beam-splitter coupling J. Two values $\Phi = 0, \pi$ of the flux are shown for equal single-mode squeezing strengths $\eta_1 = \eta_2 = 0.5$ kHz. The level of single-mode squeezing is expressed by the ratio of the smallest (ΔR^2_{sq}) and largest (ΔR^2_{a}) eigenvalues of the covariance matrix of the quadrature amplitudes recorded for each resonator. These eigenvalues indicate the amplitude variance along the squeezed and antisqueezed principal quadrature components, respectively. For $\Phi = \pi$, where the squeezed (antisqueezed) quadratures X_i (Y_i) of both resonators are coupled (cf. Fig. 2d), the slight initial imbalance in variance ratio is reduced as J increases while the value of the variance ratio remains low. In contrast, for $\Phi = 0$ – when the squeezed quadrature X_i in one resonator is coupled to the antisqueezed quadrature Y_j in the other – we observe cancellation of single-mode squeezing as the variance ratio tends to 1 with increasing J. This agrees well with theory (dashed line), where for simplicity we have assumed equal dissipation rates $\overline{\gamma} = 2.2$ kHz equal to the average of the experimental losses $\gamma_i = \{2.6, 1.9\}$ kHz, as well as equal bath occupations. Due to dynamical (optothermal) backaction, for this particular experiment the effective bath occupations $\bar{n}_1 \approx \bar{n}_2$ only differed by a few percent. **b** Two-mode squeezing observed in the cross-resonator amplitude distribution of quadratures X_1 and Y_2 for $\Phi = 0$, $J = 3.5$ kHz and $\eta_1 = \eta_2 = 0.5$ kHz. The dashed ellipse depicts the standard deviation of the principal components of the quadrature covariance matrix and shows positive correlations between X_1 and Y_2 (covariance $\sigma(X_1, Y_2) = 0.08$). **c** Covariance of the coupled quadrature pairs X_1Y_2 and Y_1X_2 as a function of J, with $\eta_1 = \eta_2 = 0.5$ kHz. No correlations are found for flux $\Phi = \pi$, when single-mode squeezing is strongest and independent of J (cf. panel a). However, for $\Phi = 0$, positive correlations $\sigma(X_1, Y_2), \sigma(Y_1, X_2) > 0$ are found when J is increased, as predicted in theory (dashed line). A trade-off between the squeezing axes rotation towards the standard two-mode squeezing limit and the decrease in the overall squeezing level as J is increased leads to a maximum covariance (although not optimal squeezing level for the rotated quadratures) at a coupling J_{opt}. For the simple theory model with equal dissipation and bath occupation that we use it is given by $J^2_{\mathrm{opt}} = (\gamma^2 - 4\eta^2)/4$. Error bars in **a** and **c** reflect statistical uncertainty and control parameter stability (Methods).

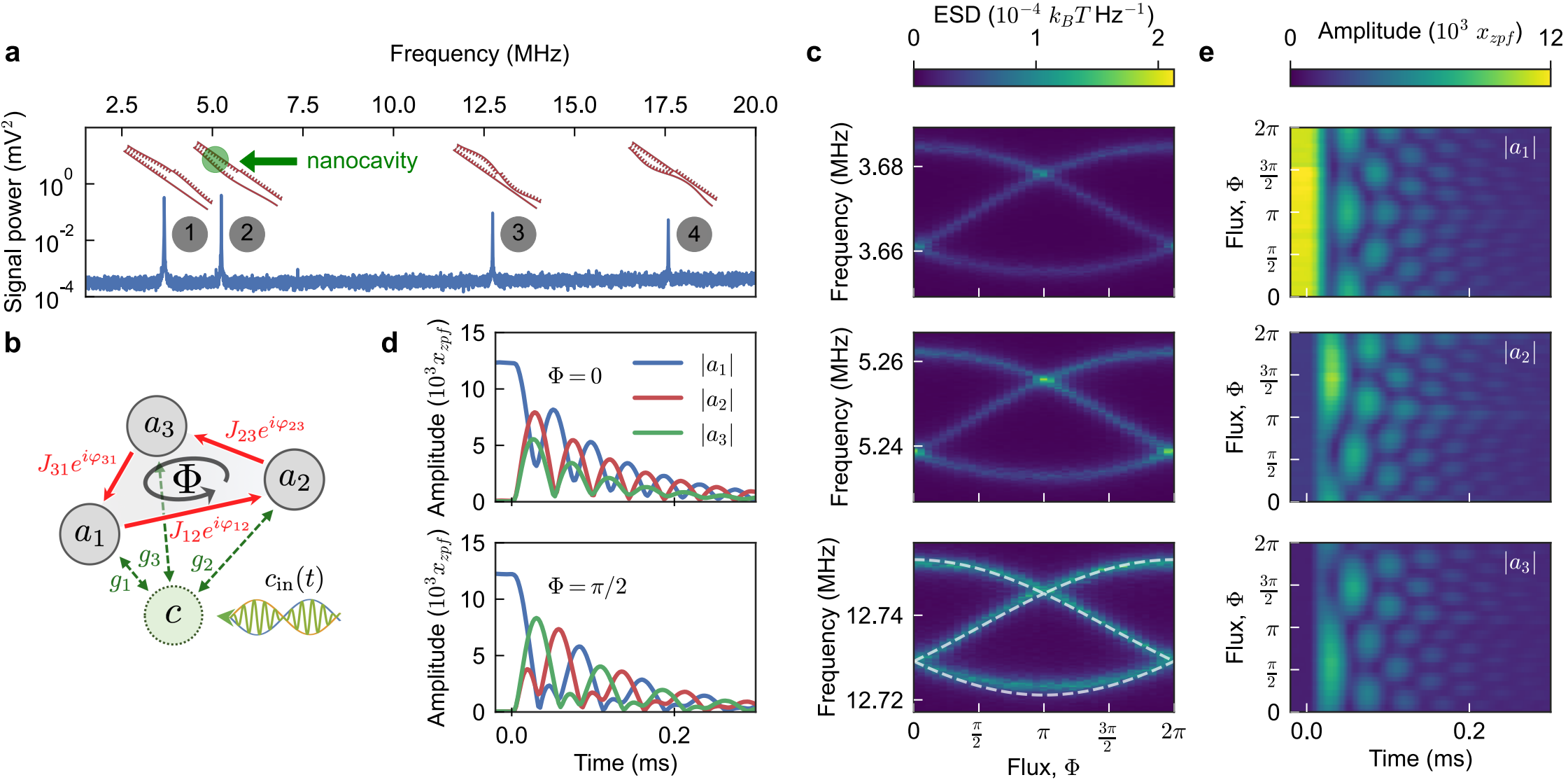
a
Frequency (MHz)
2.5
5.0
7.5
10.0
12.5
15.0
17.5
20.0
Signal power (mV^2)
10^0
10^{-2}
10^{-4}
nanocavity
1
2
3
4
b
a_3
a_2
a_1
c
Φ
$J_{31}e^{i\varphi_{31}}$
$J_{23}e^{i\varphi_{23}}$
$J_{12}e^{i\varphi_{12}}$
g_1
g_2
g_3
$c_{\rm in}(t)$
d
Amplitude ($10^3 x_{zpf}$)
$\Phi = 0$
$|a_1|$
$|a_2|$
$|a_3|$
$\Phi = \pi/2$
0.0
0.2
Time (ms)
c
ESD (10^{-4} k_BT Hz^{-1})
0
1
2
Frequency (MHz)
3.68
3.66
5.26
5.24
12.74
12.72
0
$\frac{\pi}{2}$
π
$\frac{3\pi}{2}$
2π
Flux, Φ
e
Amplitude (10^3 x_{zpf})
0
12
Flux, Φ
$|a_1|$
$|a_2|$
$|a_3|$
0.0
0.2
Time (ms)

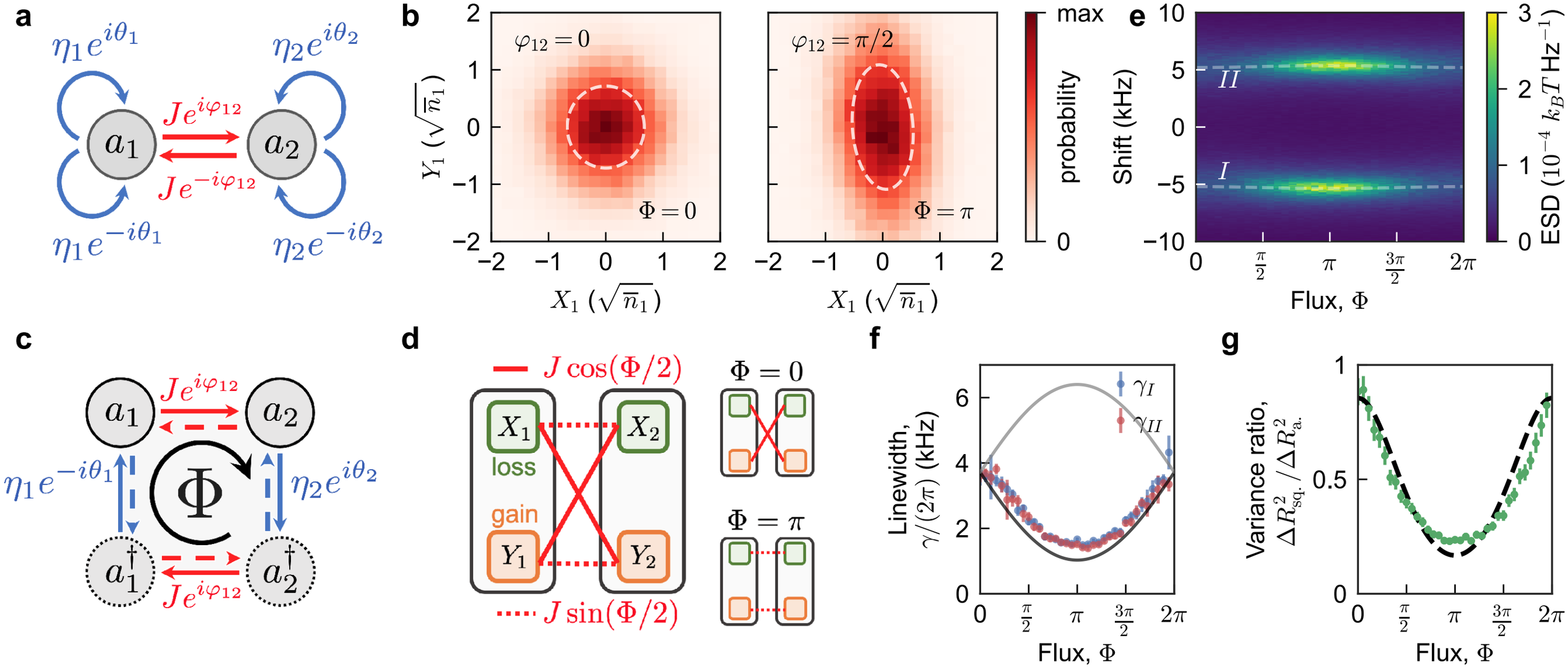
a
$\eta_1 e^{i\theta_1}$
$\eta_2 e^{i\theta_2}$
$Je^{i\varphi_{12}}$
$Je^{-i\varphi_{12}}$
a_1
a_2
$\eta_1 e^{-i\theta_1}$
$\eta_2 e^{-i\theta_2}$
b
$\varphi_{12}=0$
$\varphi_{12}=\pi/2$
$\Phi=0$
$\Phi=\pi$
$Y_1\ (\sqrt{\overline{n}_1})$
$X_1\ (\sqrt{\overline{n}_1})$
max
probability
0
e
Shift (kHz)
II
I
Flux, Φ
ESD ($10^{-4}\ k_BT\,\mathrm{Hz}^{-1}$)
c
$Je^{i\varphi_{12}}$
$\eta_1 e^{-i\theta_1}$
$\eta_2 e^{i\theta_2}$
Φ
$a_1^\dagger$
$a_2^\dagger$
d
$J\cos(\Phi/2)$
$J\sin(\Phi/2)$
X_1
X_2
Y_1
Y_2
loss
gain
$\Phi=0$
$\Phi=\pi$
f
Linewidth, $\gamma/(2\pi)$ (kHz)
γ_I
γ_{II}
Flux, Φ
g
Variance ratio, $\Delta R^2_{\mathrm{sq.}}/\Delta R^2_{\mathrm{a.}}$
Flux, Φ

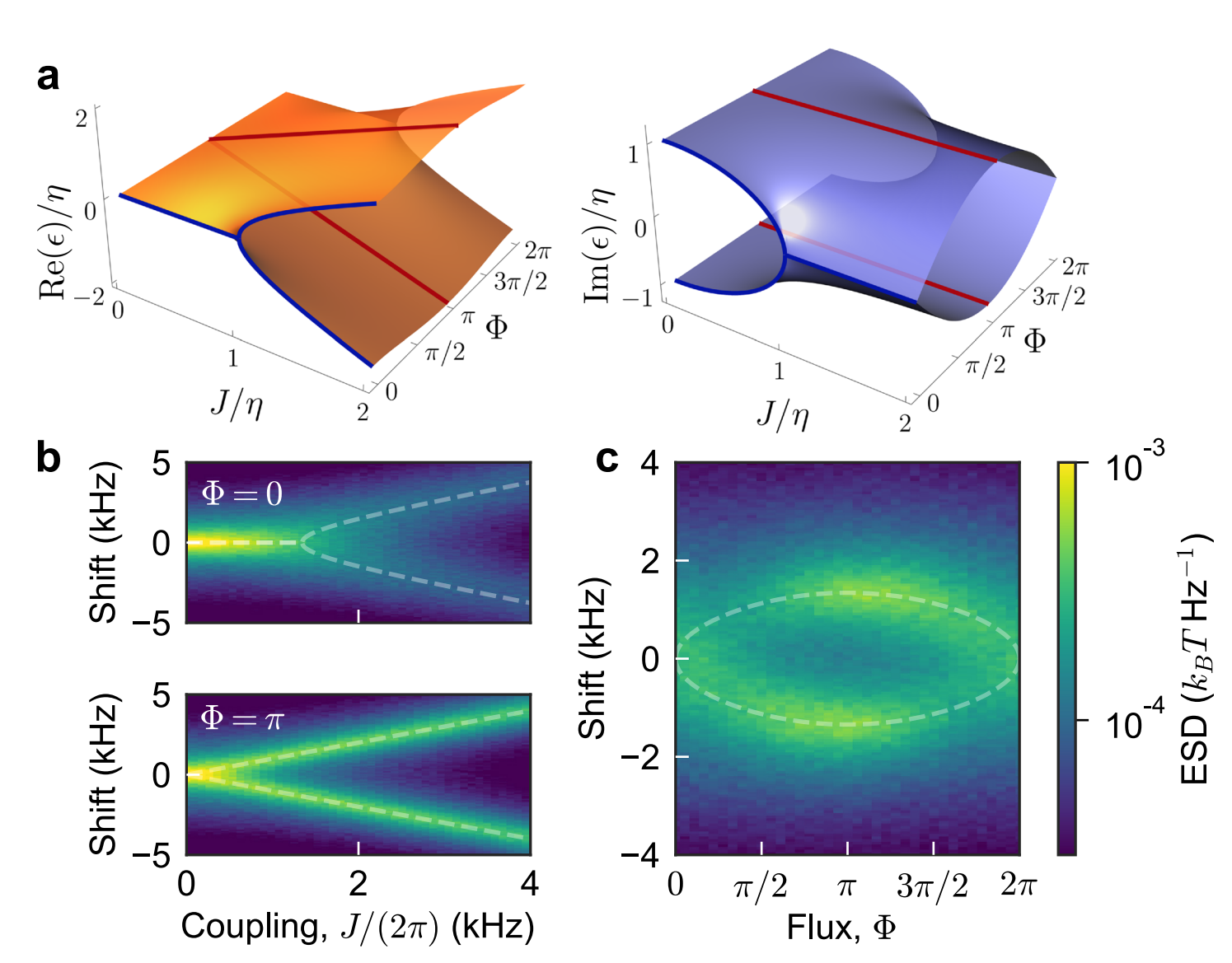
a
Re(ϵ)/η
2
0
−2
0
1
2
J/η
0
π/2
π
3π/2
2π
Φ
Im(ϵ)/η
1
0
−1
0
1
2
J/η
0
π/2
π
3π/2
2π
Φ
b
Shift (kHz)
5
0
−5
Φ = 0
Φ = π
0
2
4
Coupling, J/(2π) (kHz)
c
Shift (kHz)
4
2
0
−2
−4
0
π/2
π
3π/2
2π
Flux, Φ
10^-3
10^-4
ESD (k_B T Hz^-1)

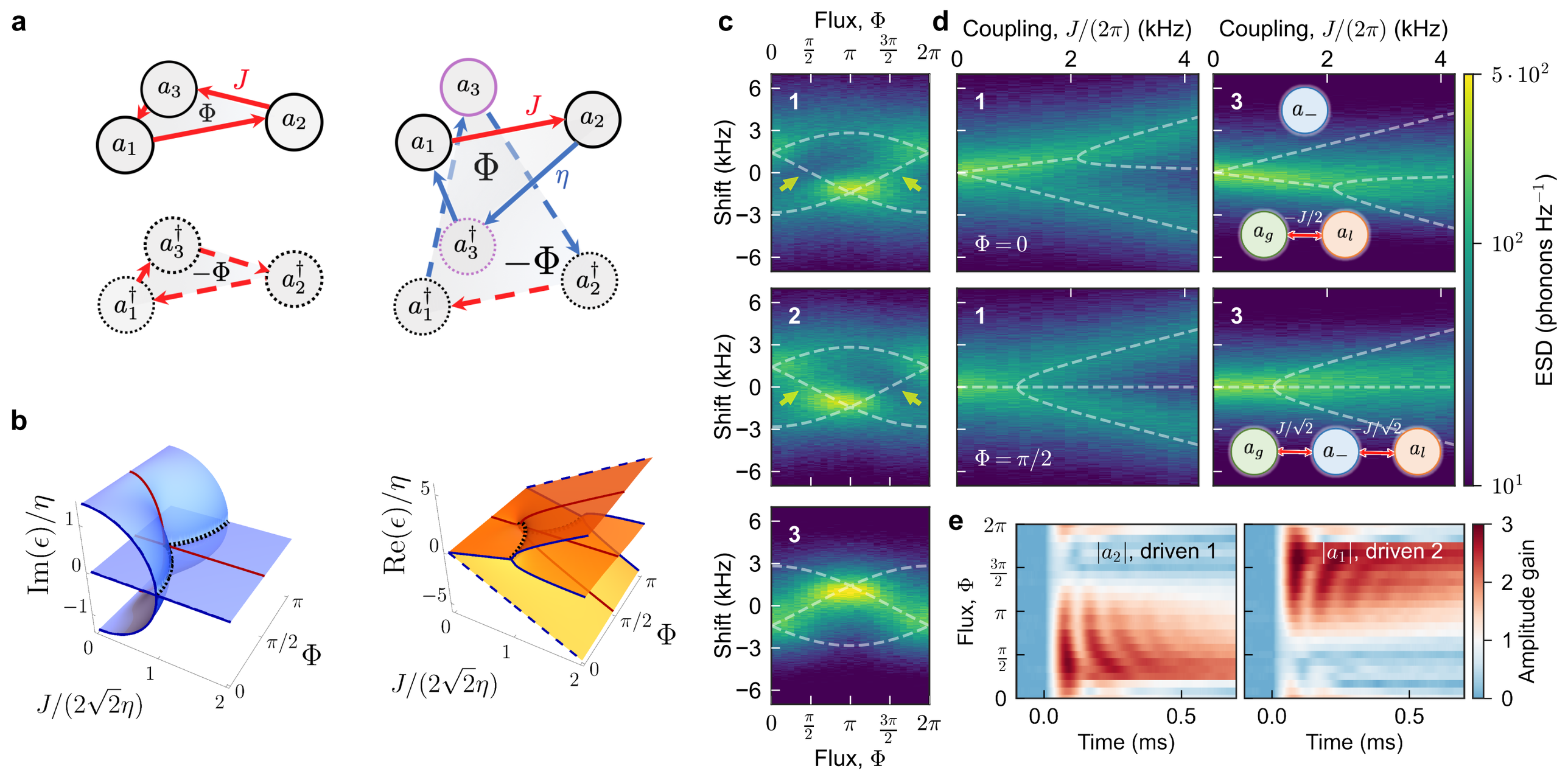
a
a_3
a_1
a_2
J
Φ
$a_3^\dagger$
$a_1^\dagger$
$a_2^\dagger$
$-\Phi$
η
b
$\mathrm{Im}(\epsilon)/\eta$
$\mathrm{Re}(\epsilon)/\eta$
$J/(2\sqrt{2}\eta)$
c
Flux, Φ
Shift (kHz)
d
Coupling, $J/(2\pi)$ (kHz)
$\Phi = 0$
$\Phi = \pi/2$
a_-
a_g
a_l
$-J/2$
$J/\sqrt{2}$
$-J/\sqrt{2}$
ESD (phonons Hz^{-1})
e
$|a_2|$, driven 1
$|a_1|$, driven 2
Flux, Φ
Time (ms)
Amplitude gain

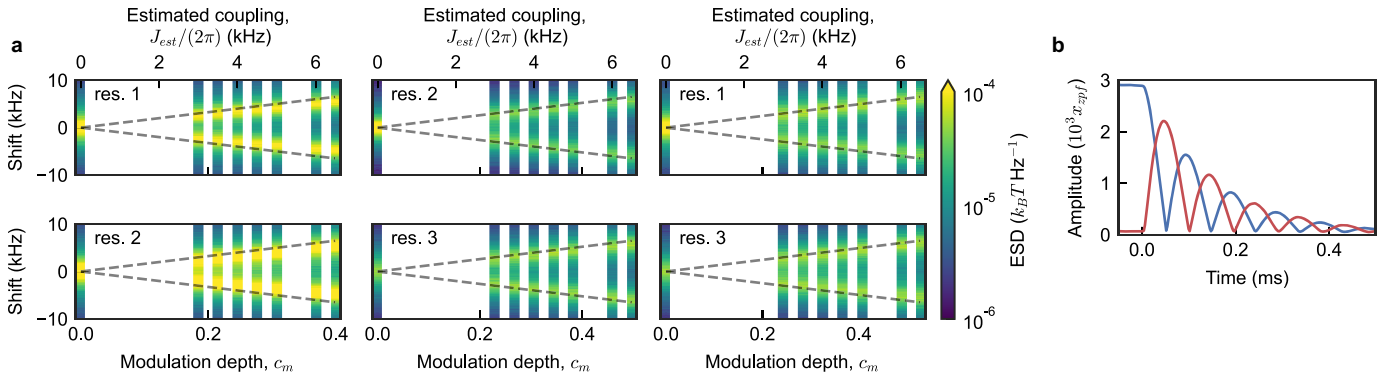
a
Estimated coupling, $J_{est}/(2\pi)$ (kHz)
Estimated coupling, $J_{est}/(2\pi)$ (kHz)
Estimated coupling, $J_{est}/(2\pi)$ (kHz)
0
2
4
6
Shift (kHz)
10
0
−10
res. 1
res. 2
res. 1
res. 2
res. 3
res. 3
0.0
0.2
0.4
Modulation depth, c_m
Modulation depth, c_m
Modulation depth, c_m
10^{-4}
10^{-5}
10^{-6}
ESD (k_BT Hz^{-1})
b
Amplitude ($10^3 x_{zpf}$)
3
2
1
0
0.0
0.2
0.4
Time (ms)

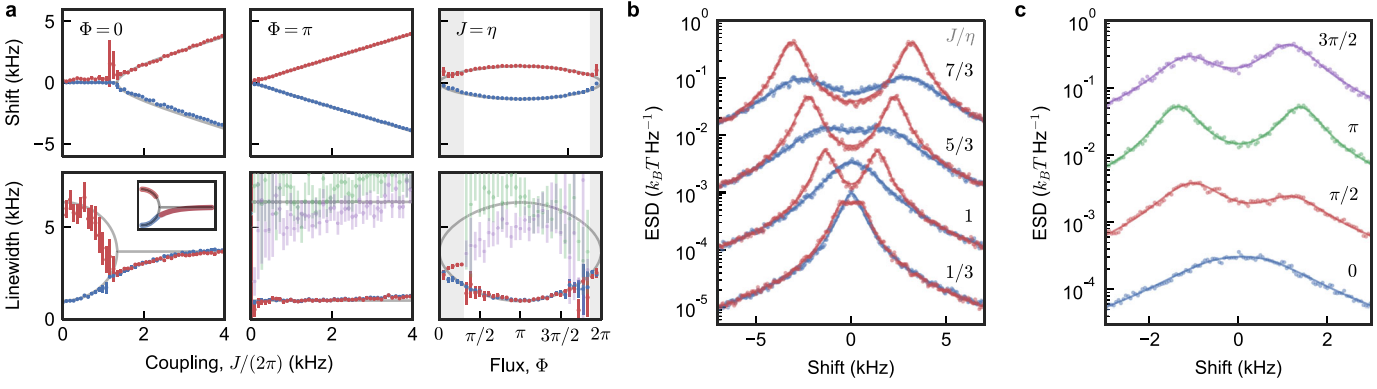
a
Φ = 0
Φ = π
J = η
Shift (kHz)
Linewidth (kHz)
Coupling, J/(2π) (kHz)
Flux, Φ
0
π/2
π
3π/2
2π
b
J/η
7/3
5/3
1
1/3
ESD (k_B T Hz^-1)
Shift (kHz)
c
3π/2
π
π/2
0
ESD (k_B T Hz^-1)
Shift (kHz)

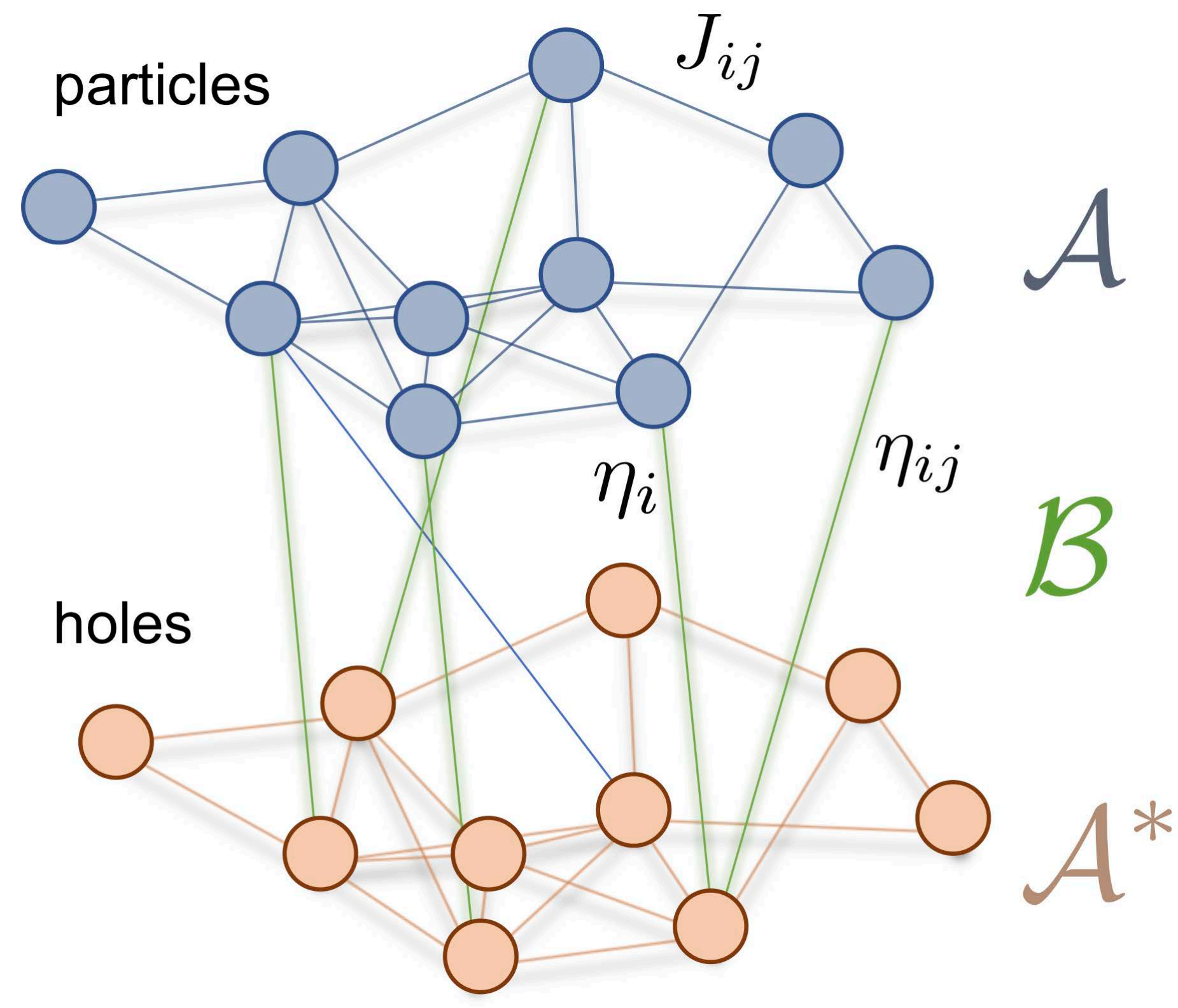
particles
J_{ij}
$\mathcal{A}$
η_i
η_{ij}
$\mathcal{B}$
holes
$\mathcal{A}^*$

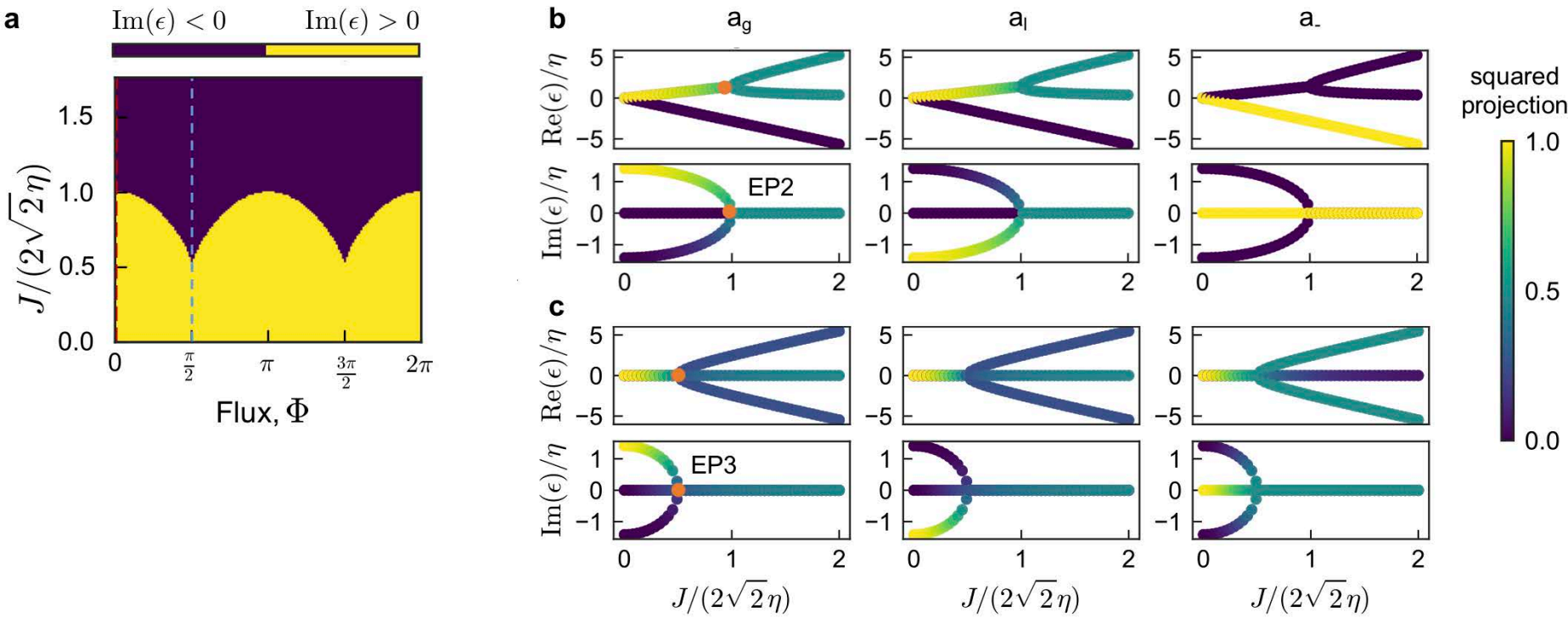
a
Im(ϵ) < 0
Im(ϵ) > 0
J/(2√2η)
Flux, Φ
b
a_g
a_l
a_-
Re(ϵ)/η
Im(ϵ)/η
EP2
c
EP3
J/(2√2η)
squared projection
1.0
0.5
0.0

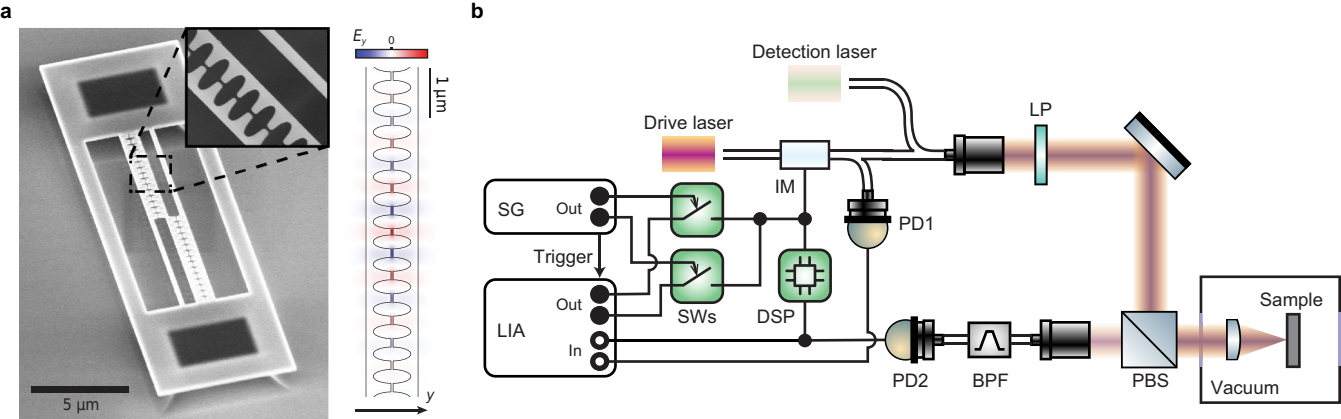
a
5 μm
E_y
0
1 μm
y
b
Detection laser
Drive laser
LP
IM
SG
Out
Trigger
PD1
SWs
DSP
LIA
Out
In
PD2
BPF
PBS
Sample
Vacuum

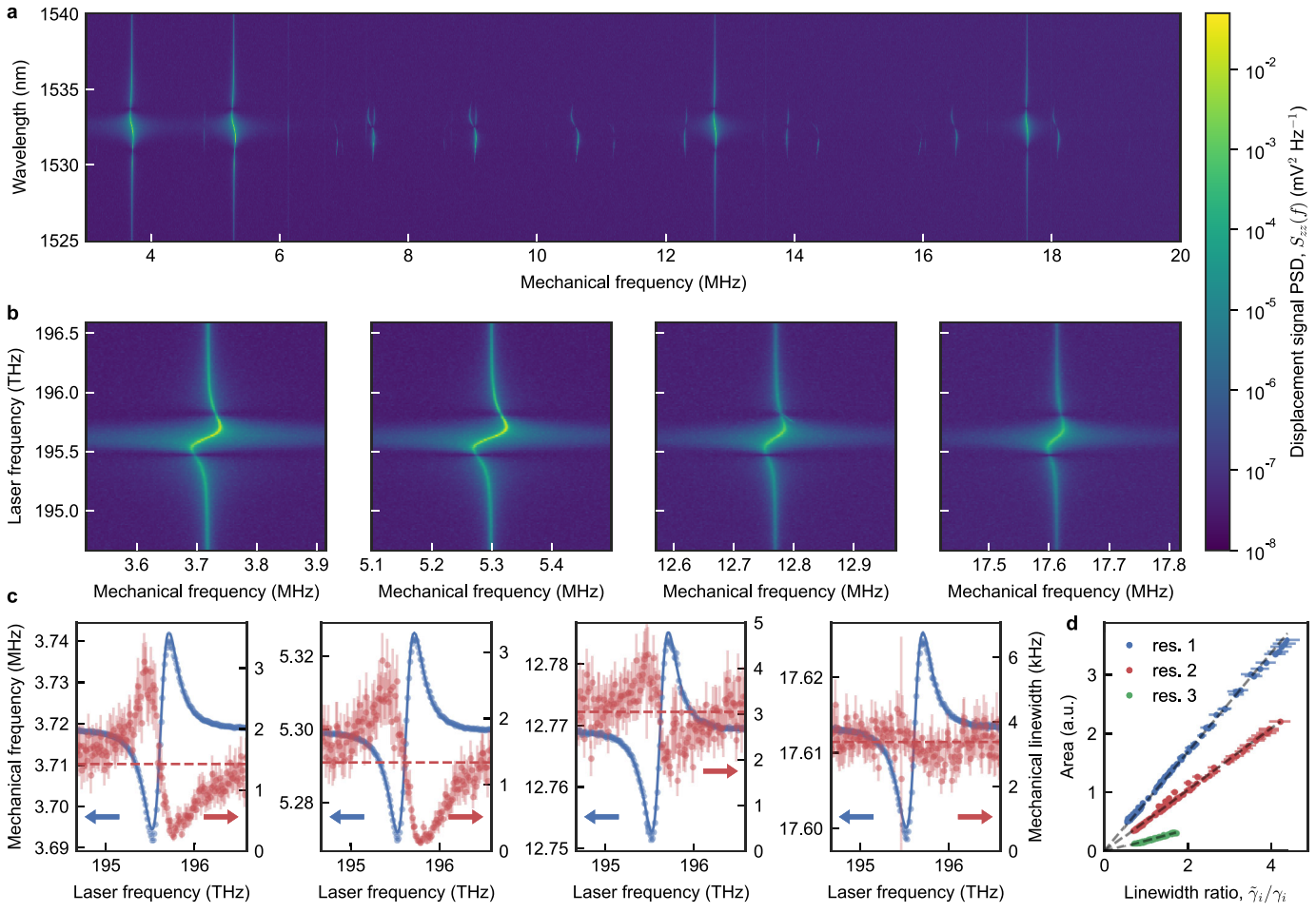
a
Wavelength (nm)
1540
1535
1530
1525
4
6
8
10
12
14
16
18
20
Mechanical frequency (MHz)
Displacement signal PSD, $S_{zz}(f)$ (mV^2 Hz^{-1})
10^{-2}
10^{-3}
10^{-4}
10^{-5}
10^{-6}
10^{-7}
10^{-8}
b
Laser frequency (THz)
196.5
196.0
195.5
195.0
3.6
3.7
3.8
3.9
5.1
5.2
5.3
5.4
12.6
12.7
12.8
12.9
17.5
17.6
17.7
17.8
Mechanical frequency (MHz)
c
Mechanical frequency (MHz)
3.74
3.73
3.72
3.71
3.70
3.69
5.32
5.30
5.28
12.78
12.77
12.76
12.75
17.62
17.61
17.60
Mechanical linewidth (kHz)
195
196
Laser frequency (THz)
d
res. 1
res. 2
res. 3
Area (a.u.)
Linewidth ratio, $\tilde{\gamma}_i/\gamma_i$

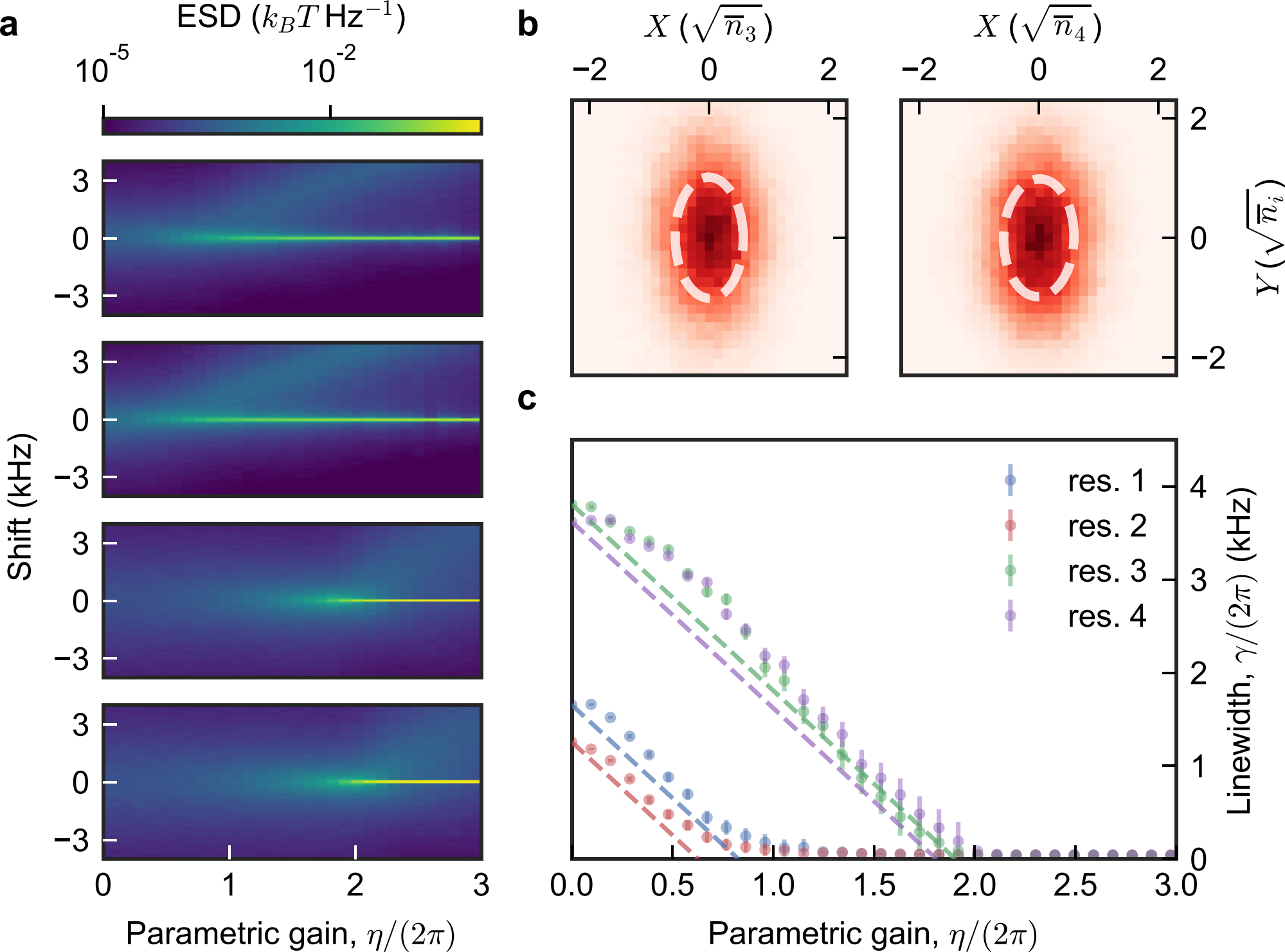
a
ESD (k_BT Hz^{-1})
10^{-5}
10^{-2}
Shift (kHz)
3
0
−3
0
1
2
3
Parametric gain, $\eta/(2\pi)$
b
$X(\sqrt{\overline{n}_3})$
$X(\sqrt{\overline{n}_4})$
−2
0
2
$Y(\sqrt{\overline{n}_i})$
c
res. 1
res. 2
res. 3
res. 4
Linewidth, $\gamma/(2\pi)$ (kHz)
0
1
2
3
4
0.0
0.5
1.0
1.5
2.0
2.5
3.0
Parametric gain, $\eta/(2\pi)$

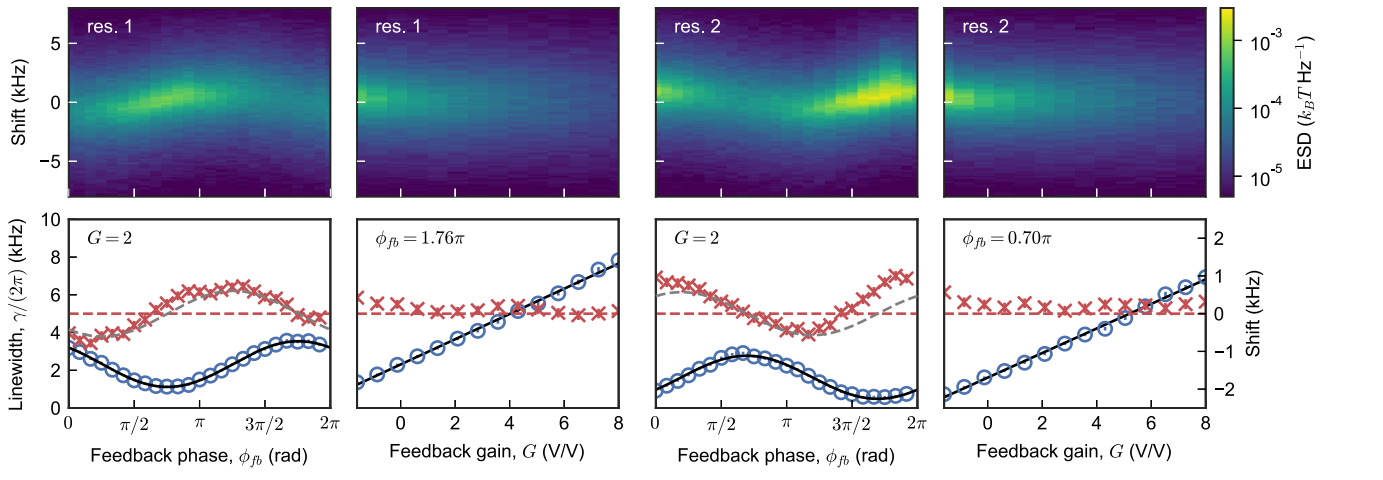
res. 1
res. 1
res. 2
res. 2
Shift (kHz)
5
0
−5
ESD (k_BT Hz^{-1})
10^{-3}
10^{-4}
10^{-5}
Linewidth, $\gamma/(2\pi)$ (kHz)
10
8
6
4
2
0
$G = 2$
$\phi_{fb} = 1.76\pi$
$G = 2$
$\phi_{fb} = 0.70\pi$
Shift (kHz)
2
1
0
−1
−2
0
$\pi/2$
π
$3\pi/2$
2π
Feedback phase, ϕ_{fb} (rad)
0
2
4
6
8
Feedback gain, G (V/V)
Feedback phase, ϕ_{fb} (rad)
Feedback gain, G (V/V)

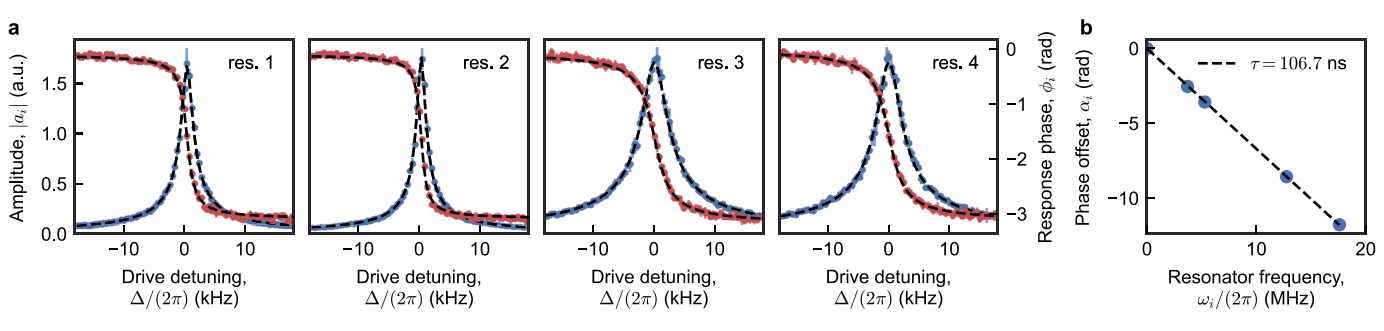
a
Amplitude, $|a_i|$ (a.u.)
res. 1
res. 2
res. 3
res. 4
Response phase, ϕ_i (rad)
Drive detuning, $\Delta/(2\pi)$ (kHz)
b
Phase offset, α_i (rad)
$\tau = 106.7$ ns
Resonator frequency, $\omega_i/(2\pi)$ (MHz)

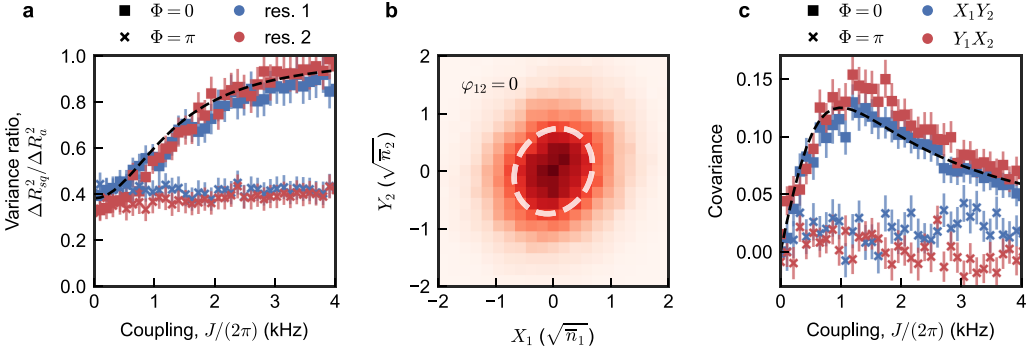
a
$\Phi = 0$
$\Phi = \pi$
res. 1
res. 2
Variance ratio, $\Delta R^2_{sq}/\Delta R^2_0$
Coupling, $J/(2\pi)$ (kHz)
b
$\varphi_{12} = 0$
Y_2 ($\sqrt{\overline{n}_2}$)
X_1 ($\sqrt{\overline{n}_1}$)
c
$\Phi = 0$
$\Phi = \pi$
X_1Y_2
Y_1X_2
Covariance
Coupling, $J/(2\pi)$ (kHz)